machines

MDPI

Article

Determining Relevant 3D Roughness Parameters for Sandblasted Surfaces: A Methodological Approach

Maxence Bigerelle [1], Eddy Chevallier [1,*], Julie Lemesle [1,2], Raphael Deltombe [1], Frederic Robache [1], Romain Vayron [1], Nadiia Zubchuk [3], Ingrid Proriol-Serre [4], Stephane Benayoun [5] and Karine Anselme [3]

[1] Laboratoire d'Automatique, de Mécanique et d'Informatique Industrielles et Humaines, LAMIH UMR CNRS 8201, Université Polytechnique Hauts-de-France, 180 Rue Joseph-Louis Lagrange, 59300 Famars, France; maxence.bigerelle@uphf.fr (M.B.); julie.lemesle@uphf.fr (J.L.); raphael.deltombe@uphf.fr (R.D.); frederic.robache@uphf.fr (F.R.); romain.vayron@uphf.fr (R.V.)
[2] Valutec, Université Polytechnique Hauts-de-France, 180 Rue Joseph-Louis Lagrange, 59300 Famars, France
[3] Institut de Science des Matériaux de Mulhouse, IS2M UMR CNRS 7361, Université de Haute Alsace, 15 Rue Jean Starcky, 68057 Mulhouse, France; nadiia.zubchuk@uha.fr (N.Z.); karine.anselme@uha.fr (K.A.)
[4] Unité Matériaux et Transformations, UMET UMR CNRS 8207, Université de Lille, 59655 Villeneuve d'Ascq, France; ingrid.proriol-serre@univ-lille.fr
[5] Laboratoire de Tribologie et Dynamique des Systèmes, LTDS UMR CNRS 5513, Ecole Centrale de Lyon, 36 Avenue Guy de Collongue, 69130 Ecully, France; stephane.benayoun@ec-lyon.fr
* Correspondence: eddy.chevallier@uphf.fr; Tel.: +33-(0)6-75-83-05-08

Abstract

This study presents a robust methodology for analyzing 3D roughness parameters to characterize sandblasted surfaces, identifying the most relevant descriptors for process optimization. Sandblasting with irregularly shaped corundum particles is performed using five grit sizes (25, 50, 90, 125, and 250 µm) and three pressure levels (2, 3, and 4 bar). The resulting surfaces are characterized through eight 3D roughness parameters: Sa, Spc, Sal, Sfd, Sdq, Sdr, Spd, and Str. A linear model of the form Q = a + b.D + d.D.P, where Q represents the roughness parameter, D is the average grit size, and P is the sandblasting pressure, is employed. For Spd, a nonlinear model, Spd = $(a + b.D + d.D.P)^2$, yields a significantly improved determination coefficient, demonstrating the model's enhanced ability to capture the complexity of the Spd parameter. The double-bootstrap analysis validates the statistical significance of all models, providing confidence intervals for each parameter. This approach emphasizes the importance of advanced 3D roughness descriptors for accurately analyzing surface textures in sandblasting processes, offering a reliable framework for surface characterization and industrial optimization.

Keywords: Ti-6A1-4V; sandblasted surfaces; roughness; 3D topography

check for updates

Academic Editor: Mirosław Rucki

Received: 29 September 2025
Revised: 27 November 2025
Accepted: 1 December 2025
Published: 5 December 2025

Citation: Bigerelle, M.; Chevallier, E.; Lemesle, J.; Deltombe, R.; Robache, F.; Vayron, R.; Zubchuk, N.; Proriol-Serre, I.; Benayoun, S.; Anselme, K. Determining Relevant 3D Roughness Parameters for Sandblasted Surfaces: A Methodological Approach. *Machines* **2025**, *13*, 1122. https://doi.org/10.3390/machines13121122

Copyright: © 2025 by the authors. Licensee MDPI, Basel, Switzerland. This article is an open access article distributed under the terms and conditions of the Creative Commons Attribution (CC BY) license (https://creativecommons.org/licenses/by/4.0/).

1. Introduction

Surface texturing through sandblasting is a widely employed technique in numerous sectors, such as in surface coatings [1–5], aerospace [6], or in the medical field (cellular biology [7–12], dental biology [13–15], ...). By projecting abrasive media at high velocities onto a material's surface, sandblasting modifies the topography, affecting critical functional properties such as adhesion [16–18], wettability [19], or tribological performance [20,21]. In the medical field, sandblasting has been largely used for improving metallic implant integration in biological tissues and notably in bone. Sandblasting creates optimal surface micro-roughness (0.5–2.0 µm), which enhances surface area and free energy, thereby promoting protein and cell adhesion [22], osteoblastic differentiation and consequently

osseointegration, a phenomenon defined as a direct structural and functional connection between the living bone and the implant surface [23,24]. However, despite many years of work, implant dentistry still faces long healing periods to achieve osseointegration, limited treatment options for some patients with only 45–65% bone-implant contact (BIC) and approximately 8% failure rate. Therefore, the goal of improving the osseointegration of microrough Ti alloys' implants provides an avenue for continued investigation in this field by improving the sandblasting process [24].

However, the relationship between sandblasting parameters and the resulting surface characteristics remains complex, involving multiple interacting variables and scale-dependent effects [25]. Recent studies confirm that the surface roughness generated by sandblasting is strongly influenced by air pressure, particle size, and projection distance. Among these, air pressure is often reported as the most dominant parameter. As instance, increasing blasting pressure on ST-37 steel plates significantly raises the average surface roughness (Sa) due to higher particle kinetic energy [26]. Similar trends were observed for SS400 steel, where the Sa increased almost linearly with pressure, regardless of abrasive mesh size [27]. For metallic and functional materials, the effect of pressure also depends on the substrate's mechanical properties. In titanium and dental alloys, three-dimensional roughness parameters (Sa, Sdq, Sdr) increase with pressure up to a critical level, beyond which excessive impacts cause micro-fracture or morphological instability [14,15,28]. For Ti-6Al-4V and pure titanium, roughness and peak density (Spd) were found to rise up to approximately 0.5 MPa before reaching a saturation point, suggesting a limit in the effectiveness of increasing pressure [14,15]. The particle size of the abrasive also plays a crucial role. Larger particles generate higher amplitude and slope values (Sa and Sdq), while smaller particles produce smoother and more uniform textures [3,28]. These effects were confirmed for Ti alloys, WC-Co coatings, and zirconia ceramics [3,14,28]. Research on Ni-Cr alloys showed that both parameters influence the efficiency of the process and the final shape of the asperities, depending on the hardness and morphology of the abrasive particles [29,30]. From a metrological perspective, the introduction of 3D surface roughness parameters (ISO 25178 [31]) has greatly improved the quantitative description of sandblasted surfaces. Recent works emphasized that parameters such as Sa, Sdq, Sdr, Spc, and Sal capture the multiscale topographic evolution more effectively than traditional 2D metrics (Ra, Rz) [14,32,33]. These studies underline the need to combine amplitude (Sa), slope (Sdq), and hybrid parameters (Sdr, Spc) to characterize the complex morphological features induced by the sandblasting process.

The primary objective of this study is to optimize the sandblasting process by identifying the ideal operational configurations required to produce surfaces with targeted roughness properties. This work proposes the development of a predictive model capable of forecasting surface roughness outcomes based on the combined influence of blasting media type, particle size distribution, and process parameters such as projection pressure. By considering a controlled selection of abrasive materials with varying grit size, the model aims not only to predict roughness parameters but also to expand the range of achievable surface textures, thereby offering a broader set of functional surface states tailored to specific industrial requirements.

To structure this study, three complementary sub-objectives have been defined. The first concerns the comprehensive characterization of sandblasted surfaces, focusing on the analysis of how process parameters influence surface roughness parameters, such as the arithmetic mean height (Sa), the auto-correlation length (Sal) or the density of peaks (Spd). Advanced surface measurement techniques and devices are employed (interferometric profilometer) to capture these parameters with high resolution and reliability. The second sub-objective addresses repeatability and uncertainty quantification, a critical aspect in

surface engineering processes where variability in experimental setups and material behavior can significantly impact results. Here, the repeatability of the sandblasting protocol is evaluated by conducting paired repetitions for each configuration, and deviations are statistically analyzed. To ensure the robustness of the findings, uncertainty estimation methods (bootstrap resampling [34,35]) are used to compute confidence intervals for the measured parameters and to assess the magnitude of experimental errors. The third sub-objective involves exploring correlations between surface roughness parameters and process variables. Given the multi-scale nature of surface topography, identifying statistically significant relationships between different roughness metrics and sandblasting conditions can provide insights into the physical mechanisms governing surface texturing. This analysis not only enhances the understanding of how process settings affect surface texturing but also contributes to the refinement of predictive models for surface functionalization processes.

For each of those sub-objectives, an analysis of variance (ANOVA) is applied to evaluate the individual and combined effects of blasting parameters on surface roughness outcomes, while correlation matrices and regression analyses are employed to examine relationships among roughness descriptors. This predictive modeling approach represents a valuable tool for industries where the ability to precisely control or predict the surface condition of sandblasted components is a key factor in product performance and quality assurance. By enabling a finer adjustment of sandblasting parameters according to the desired functional properties of the final product, the methodology developed in this study contributes to the optimization of surface engineering processes.

2. Materials and Methods

2.1. Samples Preparation

Our work being part of a study related to biomedical applications, Ti-6Al-4V (UNS standard R56400 [36]) disks of 12 mm in diameter and about 3 mm thickness were used to perform this study. Disks are cut from a 3 m length rod and then polished successively using 320, 800 and 1200 grit (Table 1) with a Tegramin-25 (Struers S.A.S., Champigny sur Marne, France). Each polishing stage was performed under water lubrication with co-rotation of the platen and specimen holder. The final surface exhibited an arithmetic mean roughness (Sa) of 0.075 $\pm$ 0.007 µm. Disks are then randomly sandblasted with corundum (Figure 1) using a Basic quattro IS Micro-sandblaster (Figure 2), both from Renfert (Renfert, Hilzingen, Germany), according to three values of pressure (2, 3 and 4 bars) and five grit sizes (25 µm, 50 µm, 90 µm, 125 µm and 250 µm). Sandblasting was applied perpendicularly to the surface at a distance of 5 cm. The abrasive jet was swept laterally across the surface, requiring approximately five passes to fully treat each specimen due to their small size. The treatment of a single specimen took only a few seconds. Each condition was reproduced twice, resulting in a total of 30 specimens for analysis.

Table 1. Polishing parameters applied at each stage of the process. Each polishing step was carried out in co-rotation of the platen and specimen holder under water lubrication. The procedure resulted in a surface roughness of 0.075 $\pm$ 0.007 µm.

Grit	Load (N)	Table Speed (rpm)	Holder Speed (rpm)	Duration
320	25	300	150	2 min30
800	20	300	150	2 min30
1200	15	200	150	5 min

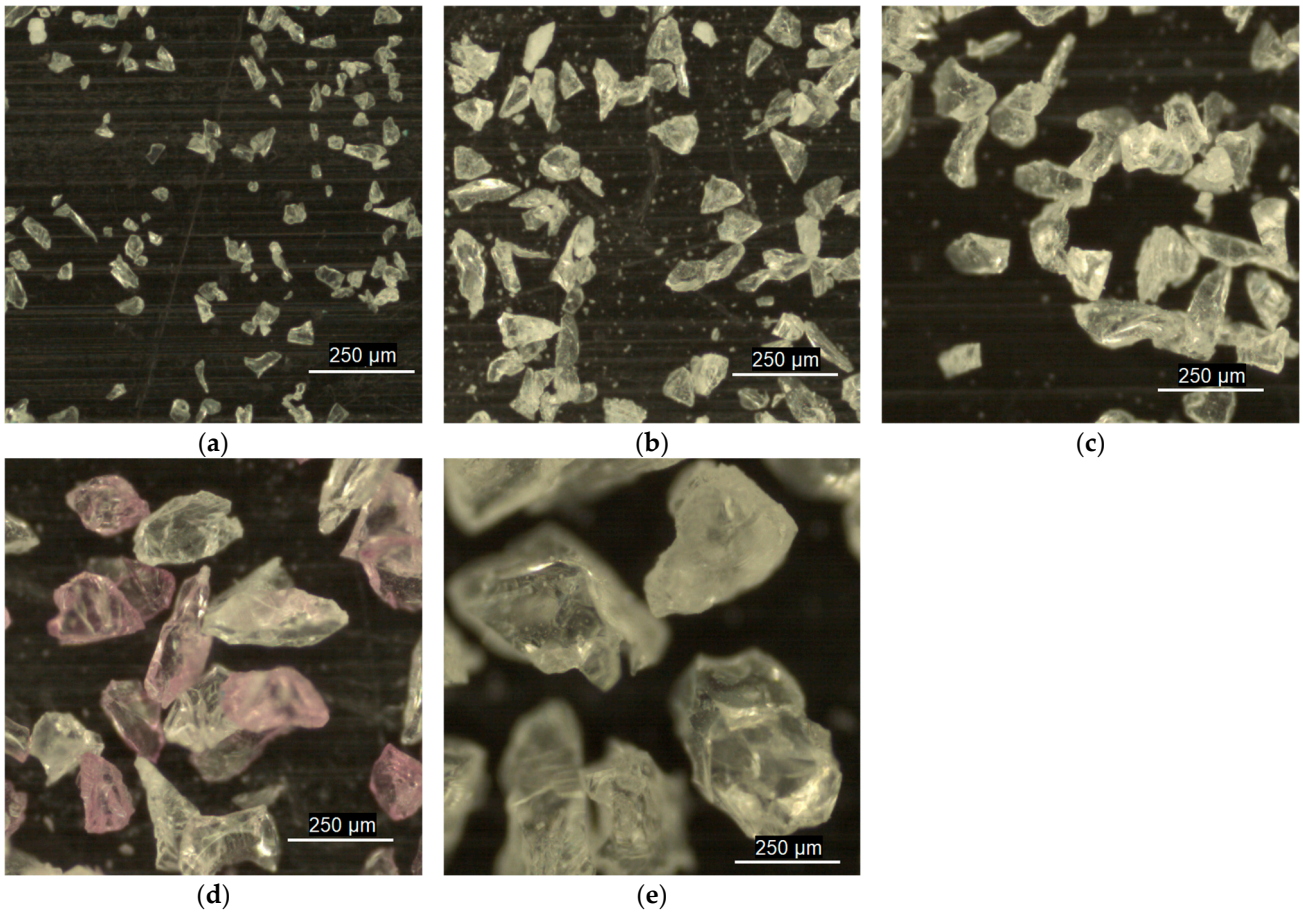


Figure 1. Pictures of corundum grains (Al_2O_3) obtained using an Infinite focus G5 microscope from Alicona (Alicona Imaging GmbH, Raaba, Austria). The average grit size is (**a**) 25 µm, (**b**) 50 µm, (**c**) 90 µm, (**d**) 125 µm and (**e**) 250 µm.

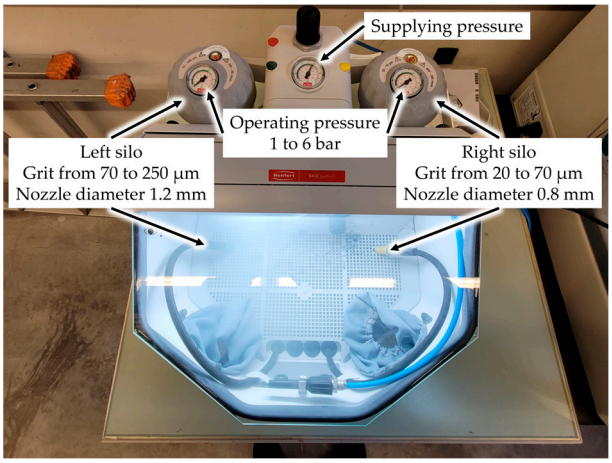


Figure 2. Basic quattro IS Micro-sandblaster (Renfert, Hilzingen, Germany) [37].

The sandblaster is made of two 1 L silos, each connected to a dedicated steel nozzle. The left silo is fitted with a 1.2 mm (0.047 in) diameter nozzle and can contain abrasive grains sized from 70 to 250 µm, while the right silo is fitted with a 0.8 mm (0.031 in) diameter nozzle and can contain grains sized from 25 to 70 µm. Each silo is connected to its own barometer for jet pressure control, with a working pressure range from 1 to 6 bar and a maximum flow rate of 98 L/min (3.46 cfm). The sandblaster functions in an open circuit, meaning the abrasive grains are expelled and not reused after projection. The system

is supplied by a 500 L air compressor operating at 8 bar, which guarantees a stable and continuous air supply during the entire operation time.

2.2. Three-Dimensional Topographic Data Pre-Processing

The 3D topography of each of the 30 produced samples is measured at 30 different randomly selected positions, sized 1 mm by 1 mm, resulting in a total of 900 images for analysis. Measurements are performed using an interferometer (Newview 7300, Zygo, Middlefield, CT, USA) with a x20 lens to guarantee high resolution images and are then processed by the software Mountain® 10 (Digital Surf, Besançon, France). Each of these topographic measurements (topographic maps) are systematically preprocessed then to correct instrumental artifacts, remove spurious data points, and separate the global form from the surface texture. The procedure consisted of the following steps:

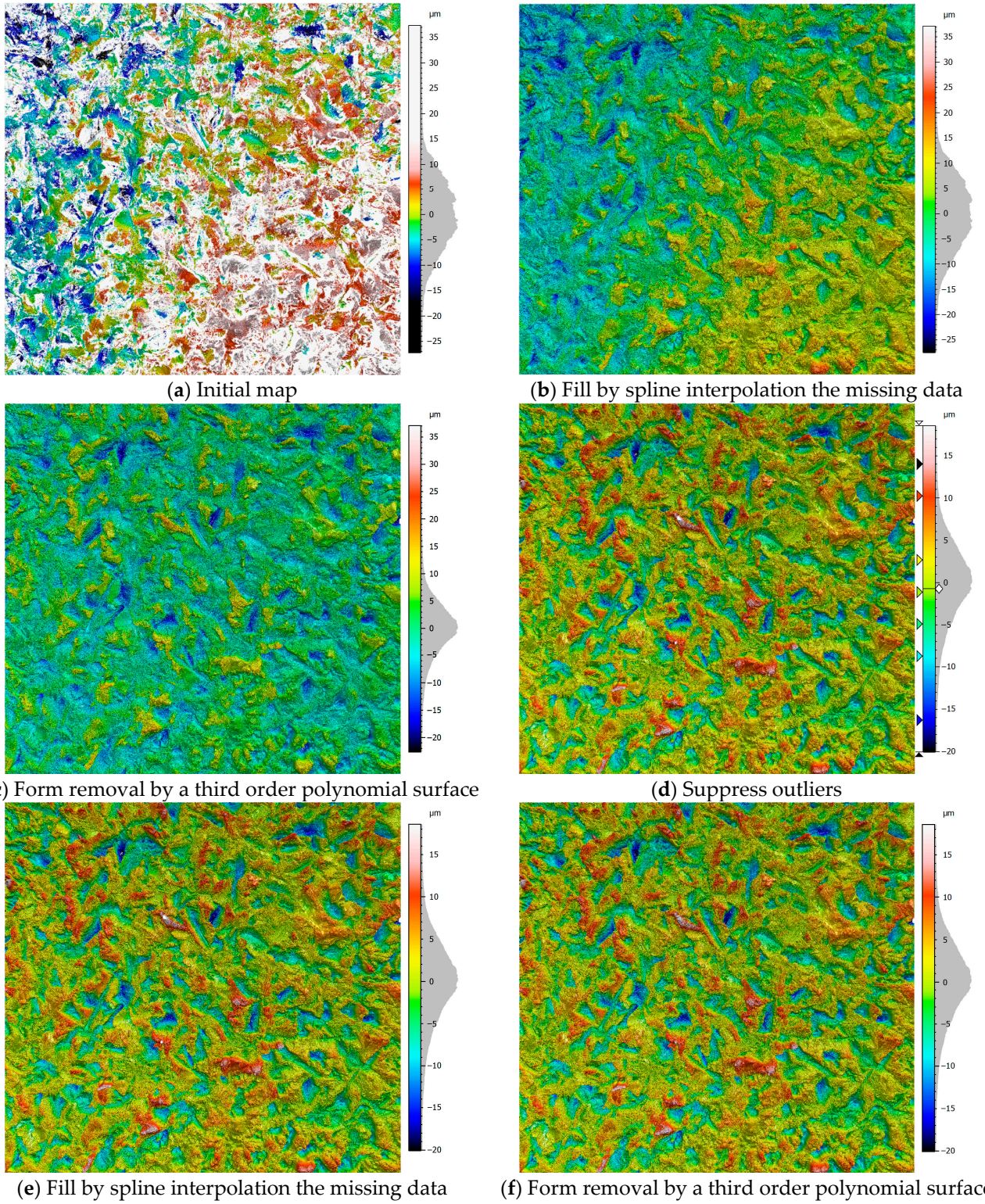
1. Initial Map (Figure 3a). The raw topographic map was imported directly from the measurement instrument (format: OPDx). Heights were expressed in µm. Before any treatment, the map was visually inspected to ensure the absence of acquisition errors (missing scan lines, saturation artifacts, misalignment or stitching error).
2. Filling Missing Data (Figure 3b). Missing or invalid points (e.g., masked areas, saturated or unmeasured pixels) were filled using spline interpolation. A bicubic (or tensor) spline was applied to ensure smooth continuity of the first derivatives and to minimize artificial oscillations. This step provided a complete and continuous height field, required for subsequent global operations such as form removal.
3. Form Removal (Figure 3c). The global form (slow-varying background) was estimated and removed by fitting a third-order polynomial surface using least squares:

$$z_{Form}(x,\ y) = \sum_{i=0}^{3} \sum_{0}^{3-i} a_{i,j} x^i y^j \quad (1)$$

The fitted background $z_{form}(x,y)$ was subtracted from the interpolated map to obtain the detrended surface. The choice of a third-order polynomial allows removal of large-scale curvature without affecting the relevant micro- and meso-scale roughness features.
4. Outlier Suppression (Figure 3d). Extreme values in the height distribution—typically caused by dust particles or measurement noise—were eliminated by retaining only the data points between the 0.01% and 99.99% percentiles of the height histogram. Formally, if P_p denotes the p-th percentile, only heights (z) satisfying:

$$P_{0.01\%} \leq z \leq P_{99.99\%} \quad (2)$$

were kept. Points outside this interval were marked as missing and handled in the next step. This strict filtering window efficiently removes rare, non-physical outliers while preserving the genuine surface variability.
5. Second Filling (Figure 3e). After outlier removal, the newly missing data points were again filled by spline interpolation, using the same method as before. This second interpolation ensures smooth continuity and prevents edge effects during the following form correction.
6. Second Form Removal (Figure 3f). A second polynomial form removal (order 3) was applied to the corrected surface to eliminate any residual background curvature introduced during the previous interpolation or filtering steps. This iteration ensures that the final map contains only the surface texture and roughness components relevant for analysis.



(**a**) Initial map (**b**) Fill by spline interpolation the missing data

(**c**) Form removal by a third order polynomial surface (**d**) Suppress outliers

(**e**) Fill by spline interpolation the missing data (**f**) Form removal by a third order polynomial surface

Figure 3. Sequential illustration of the preprocessing workflow applied to the 3D topography of a sandblasted Ti-6Al-4V surface (grit size 250 µm at 3 bar pressure). The six maps show the progressive correction of the raw topography prior to roughness parameter computation. The resulting map represents the corrected topography, centered on the roughness signal and suitable for quantitative parameter analysis. (**a**) Initial map: raw 3D surface as measured, showing the global curvature and potential acquisition artifacts (missing lines, saturated pixels). (**b**) Spline interpolation: first correction step consisting of filling non-measured or invalid points using bicubic spline interpolation to reconstruct a continuous height field while preserving the local slope continuity. (**c**) First form removal: subtraction of a third-order polynomial surface fitted by least squares to remove the long-

wavelength curvature and isolate the local roughness component. (**d**) Outlier suppression: removal of non-physical height values (dust particles, optical spikes) by restricting the height distribution to the [0.01%, 99.99%] percentile range of the histogram. The extreme points beyond these thresholds are marked as missing. (**e**) Second interpolation: spline interpolation applied again to fill the missing data created during outlier removal, ensuring smooth continuity of the surface and preventing boundary effects in the final detrending. (**f**) Second form removal: a final third-order polynomial fit and subtraction to eliminate any residual background curvature introduced during previous steps.

Repeating the interpolation and form-removal sequence (fill → detrend → filter → fill → detrend) reduces interpolation bias and enhances the separation between long-wavelength form and the texture of interest. A third-order polynomial provides a suitable compromise: lower orders (e.g., 1) leave residual curvature, whereas higher orders may suppress meaningful roughness components. The selected order can be adapted to the specimen geometry and measurement scale. Percentile filtering between 0.01% and 99.99% effectively eliminates isolated outliers; for datasets containing a greater proportion of spurious values, wider thresholds (e.g., 0.1–99.9%) or robust statistical filters based on interquartile range may be more appropriate. Spline interpolation ensures slope continuity more effectively than bilinear interpolation, although it may slightly smooth micro-textures.

To verify the validity of the process, surfaces must be visually inspected before and after each step, and key roughness parameters (Sa, Sq, Sdr, fractal dimension, Smr2, Vvc) compared to confirm that their physical meaning is preserved. Complementary, Power Spectral Density (PSD) analysis must also be conducted to ensure that no relevant frequency bands are lost during detrending or interpolation.

2.3. Analysis Parameters

The Sa representative surfaces obtained for each grit size, at an identical pressure of 3 bars, are presented in Figure 4. The representative surface here is the surface which presents a Sa value closest to the median of the Sa values calculated over all the 60 measurements made. The representative surfaces for the other studied cases are relied in Appendix A.

Eight normalized parameters, according to the standard ISO 25178 [35], have been selected in order to cover different topographical aspects of the studied surfaces and are listed as follow:

- Sa—arithmetic mean height, which gives a global view of the average roughness;
- Sal—auto-correlation length, which indicates characteristic length of patterns;
- Str—texture aspect ratio, which measures the isotropy, or the anisotropy, of the surface;
- Sdq—root mean square gradient, which indicates the average value of the surface variations;
- Sdr—developed interfacial area ratio, which quantifies the real surface area according to a flat plane;
- Spd—density of peaks, which represents the number of peaks by surface unit;
- Spc—arithmetic mean peak curvature, which characterizes the shape of asperities;
- Sfd—fractal dimension, which measures the surface complexity at different scales.

All those parameters reflect the main topographical characteristics influenced by the sandblasting process, especially for global and local roughness, isotropic patterns, shape of summits and multi-scale complexity such as fractal variations.

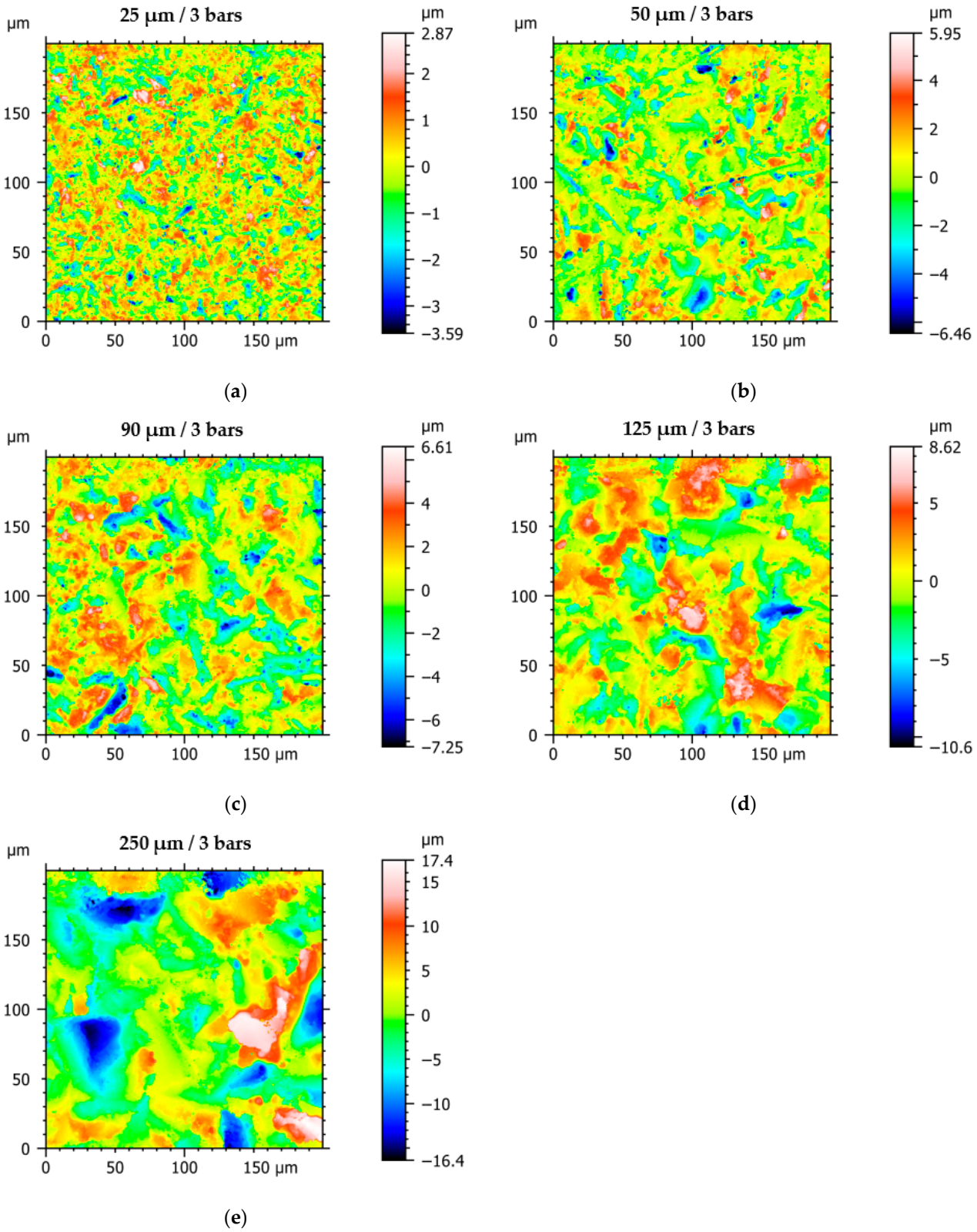


Figure 4. Representative surfaces obtained for a grit size of (**a**) 25 µm, (**b**) 50 µm, (**c**) 90 µm, (**d**) 125 µm and (**e**) 250 µm, at a pressure of 3 bars. It is clearly observable that the grit size has a direct impact, both on the depth of penetration and on the width of the created patterns.

3. Results and Modeling

The analysis of all the selected parameters is resumed in Table 2. For each sandblasting condition, the eight parameters are estimated by calculating their respective mean and

standard error on the N retained measurements. The evolution of the Sa parameter is represented in Figure 5. The evolution of the other parameters is relied in the Appendix B.

Table 2. Respective mean and standard error (SE) of the eight selected topographical parameters according to the pressure, P, and the grit size media, D, computed on the N retained measurements from a total of 60.

D (µm)	P (bar)	N	Sa (µm)	Sal (µm)	Str	Sdq	Sdr (%)	Spd (10^{-3}/µm^2)	Spc (1/µm)	Sfd
			Mean ± SE							
	2	52	0.53 ± 0.01	3.07 ± 0.13	0.97 ± 0.01	1.21 ± 0.01	43.64 ± 0.30	53.98 ± 0.38	4.26 ± 0.08	2.886 ± 0.002
25	3	60	0.59 ± 0.01	4.08 ± 0.12	0.98 ± 0.01	1.25 ± 0.01	45.21 ± 0.27	45.85 ± 0.35	4.36 ± 0.08	2.878 ± 0.002
	4	53	0.64 ± 0.01	4.58 ± 0.13	0.95 ± 0.01	1.33 ± 0.01	48.90 ± 0.29	40.33 ± 0.37	4.72 ± 0.08	2.866 ± 0.002
	2	60	1.03 ± 0.01	6.68 ± 0.12	0.90 ± 0.01	1.74 ± 0.01	69.16 ± 0.27	27.24 ± 0.35	6.58 ± 0.08	2.816 ± 0.002
50	3	60	1.15 ± 0.01	8.16 ± 0.12	0.80 ± 0.01	1.82 ± 0.01	73.09 ± 0.27	24.30 ± 0.35	7.18 ± 0.08	2.800 ± 0.002
	4	60	1.21 ± 0.01	10.20 ± 0.12	0.85 ± 0.01	1.77 ± 0.01	70.42 ± 0.27	24.81 ± 0.35	6.95 ± 0.08	2.798 ± 0.002
	2	60	1.28 ± 0.01	9.81 ± 0.12	0.84 ± 0.01	1.85 ± 0.01	74.78 ± 0.27	25.29 ± 0.35	7.33 ± 0.08	2.798 ± 0.002
90	3	59	1.49 ± 0.01	11.57 ± 0.12	0.88 ± 0.01	1.96 ± 0.01	79.21 ± 0.28	21.08 ± 0.35	8.19 ± 0.08	2.770 ± 0.002
	4	60	1.60 ± 0.01	13.02 ± 0.12	0.90 ± 0.01	1.99 ± 0.01	80.07 ± 0.27	19.19 ± 0.35	8.46 ± 0.08	2.758 ± 0.002
	2	60	1.90 ± 0.01	11.94 ± 0.12	0.92 ± 0.01	2.34 ± 0.01	89.68 ± 0.27	15.42 ± 0.35	9.61 ± 0.08	2.738 ± 0.002
125	3	60	2.19 ± 0.01	14.44 ± 0.12	0.92 ± 0.01	2.33 ± 0.01	93.08 ± 0.27	13.40 ± 0.35	10.42 ± 0.08	2.713 ± 0.002
	4	60	2.44 ± 0.01	15.43 ± 0.12	0.92 ± 0.01	2.39 ± 0.01	94.28 ± 0.27	10.86 ± 0.35	11.32 ± 0.08	2.685 ± 0.002
	2	60	3.17 ± 0.01	18.89 ± 0.12	0.92 ± 0.01	2.63 ± 0.01	98.67 ± 0.27	6.51 ± 0.35	14.66 ± 0.08	2.620 ± 0.002
250	3	60	3.65 ± 0.01	21.25 ± 0.12	0.92 ± 0.01	2.79 ± 0.01	106.32 ± 0.27	5.73 ± 0.35	16.09 ± 0.08	2.605 ± 0.002
	4	60	4.22 ± 0.01	24.63 ± 0.12	0.90 ± 0.01	3.14 ± 0.01	125.87 ± 0.27	6.28 ± 0.35	18.30 ± 0.08	2.606 ± 0.002

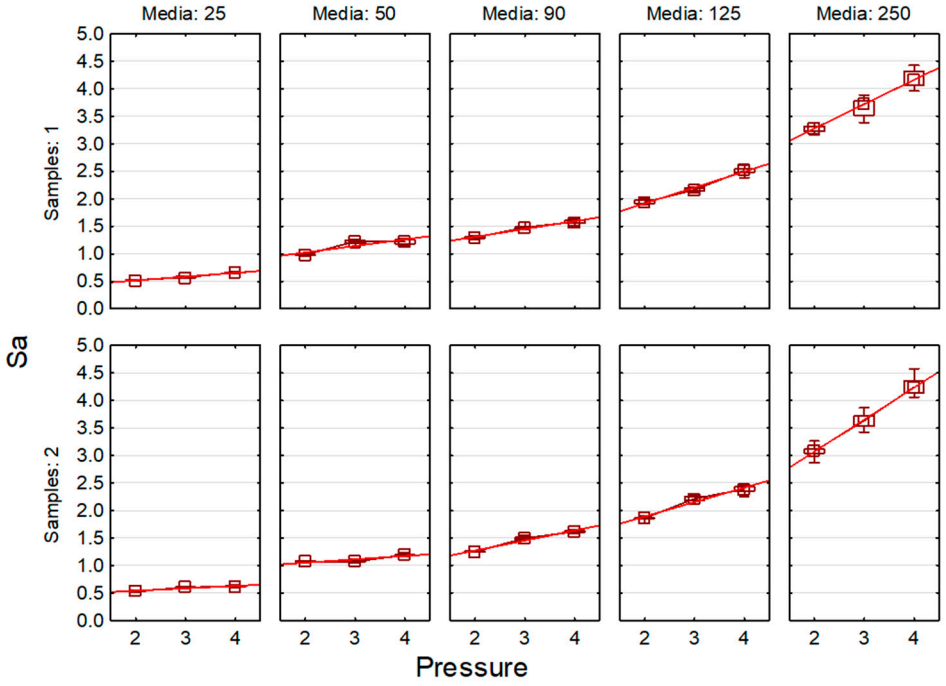


Figure 5. Evolution of the Sa (µm) according to the pressure (bar) and the grit size (µm), for each sample. Each series of three points is linearly fitted. The box plots show the statistical parameters, respectively, the 1st and 9th decile and the 1st, 2nd and 3rd quartile, obtained from 60 measured images.

In order to build an interpretative model of the evolution of these parameters with the sandblasting parameters, the influence of the grit size, D, and the pressure, P, need to be discussed:

1. The abrasive particles size used in sandblasting processes have a specific role on the making of roughness: the greater the size, the more important the irregularities on the surface. Bigger particles are heavier, and so have more inertia and more energy allowing them to penetrate deeper into the surface. This leads to deeper crater and more highlighted irregularities. Furthermore, due to their size, the surface distribution of the impacts can become more heterogeneous, which can lead to rougher surfaces with various structures.

2. In sandblasting processes, pressure gives their kinetic energy to the particles. Higher pressure leads to higher velocity of the particles, which leads to higher impacts. High energy impacts lead to bigger deformations and so increase the roughness. This also leads to let particles to penetrate deeper into the surface with the same consequences than with the grit size. A higher pressure can also lead to a higher impact rate by surface unit, increasing proportionally the roughness.

From those considerations, a linear model describing the evolution of the Sa with the sandblasting parameters is build and is mathematically expressed by (3), where a, b, c and d are coefficients to be determined:

$$Sa = a + b.D + c.P + d.D.P \quad (3)$$

The terms b.D and c.P show, respectively, the direct impact of the grit size and the pressure on roughness: they both indicate a linear and independent increasing. The term d.D.P couples grit size and pressure, indicating the effect amplification from a parameter on the other one. Finally, the term a seems to be the initial roughness of the surface before any sandblasting. This term can thus be interpreted as a baseline for evaluating the effect of the other variables.

4. Evaluation of the Regression Coefficients and Their Uncertainties

The values of the coefficients a, b, c and d are determined using a least square regression based on the model defined by (3), and are resumed in Table 3. The results indicate an excellent model fit, with a coefficient of determination R^2 = 0.9927, meaning that 99.27% of the variance in Sa is explained by the model.

Table 3. Computation of the regression coefficients a, b, c and d using the least square regression model defined by (3). The value of each parameter is accompanied by their respective standard error (SE), *p*-value with a level of confidence of 95% and significance appreciation.

	Value	**SE**	***p*-Value**	**Significance**
a	0.383	0.029	$<10^{-4}$	High
b	0.0070	0.0002	$<10^{-4}$	High
c	−0.011	0.009	0.23	Null
d	0.0021	7×10^{-5}	$<10^{-4}$	High

Table 3 highlights that the value of the coefficient c is not significant. To confirm this result, a residuals bootstrap analysis is performed on this coefficient—a description of the bootstrap methods is presented in Appendix C. The histogram of the generated c bootstrap values is represented in Figure 6. The *p*-value, p_c, deduced by the bootstrap analysis is 0.435, confirming that the coefficient c is not significant and can be removed from the model equation. This result leads to conclude that pressure alone, when the grit size tends to zero, does not have a direct influence on the average roughness. Inversely, the coefficient b being significant leads to conclude that the grit size alone, when pressure tends to zero, does still have a direct influence on the average roughness. This result also reinforces the importance of the coupling between pressure and grit size on the sandblasting process.

Note that a complementary study, presented in Appendix D, has been performed by applying the same regression model with the same bootstrap analysis method on the 86 roughness parameters from the standard ISO 25178 [35] and leads to conclude that the coefficient c remains consistently insignificant.

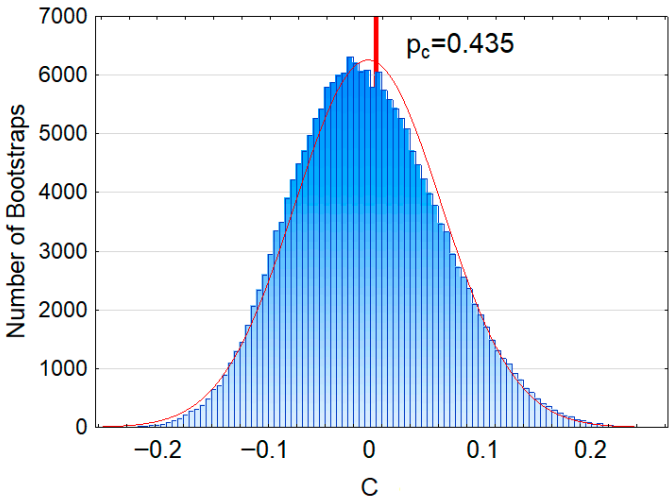


Figure 6. Bootstrap analysis of the *p*-values confirming that the regression coefficient c is not significant.

Removing the coefficient c from (3) leads to (4), simplifying the analysis and enhancing its clarity and predictive accuracy. Focusing on the significant coefficients a, b, and d eliminates unnecessary complexity and reduces the risk of overfitting. This approach allows a clearer interpretation of the relationship between process parameters and surface roughness, providing a more accurate depiction of the sandblasting mechanism. The next step involves recalculating the coefficients a, b, and d for this new model to finalize the quantitative understanding of how particle diameter and its interaction with pressure influence surface characteristics

$$Sa = a + b.D + d.D.P \tag{4}$$

The results of the estimation of the coefficients a, b and d for each of the eight roughness parameters are resumed in Table 4.

Table 4. Computation of the regression coefficients a, b and d using the least square regression model defined by (4), for each of the eight roughness parameters. The value of each regression coefficient is accompanied by their 95% confidence interval (CI) obtained by bootstrap, and each roughness parameter is accompanied by their respective coefficient of determination R^2, showing that removing the c parameter simplifies the model while maintaining its efficiency and statistical relevance.

	a	**b ($\times 10^{-3}$)**	**d ($\times 10^{-3}$)**	**R^2**
		Mean [95% CI]		
Sa	0.38 [0.32 0.44]	5.40 [5.38 5.42]	2.10 [1.99 2.27]	0.992 [0.991 0.994]
Sal	3.89 [2.78 4.94]	33 [11 56]	13 [6 20]	0.967 [0.944 0.987]
Str	-	-	-	-
Sdq	1.33 [1.18 1.47]	3.80 [0.60 6.70]	0.90 [−0.10 1.90]	0.927 [0.875 0.970]
Sdr	52.08 [43.94 59.41]	0.12 [−0.04 0.27]	45.10 [6.50 94.80]	0.876 [0.778 0.952]
Spd	0.039 [0.033 0.046]	−0.10 [−0.20 0.01]	0.01 [−0.05 0.03]	0.767 [0.557 0.921]
Spc	3.70 [3.17 4.27]	30.30 [15.10 45.00]	6.90 [2.30 11.90]	0.985 [0.972 0.994]
Sfd	2.87 [2.85 2.89]	−0.9 [−1.2 −0.5]	−0.08 [−0.20 0.02]	0.952 [0.908 0.979]

The use of bootstrap for calculating the confidence intervals highlights that all the coefficients are highly significant, and removing the c parameter simplifies the model while maintaining its statistical and physical relevance, allowing us to focus on the most impactful effects. The confidence intervals of the determination coefficients R^2 further validate the statistical robustness of the model, confirming the dominant influence of particle diameter

and its interaction with pressure on roughness. However, that regression model seems less relevant regarding to the Spd. This parameter therefore requires special attention. The graphical comparison between measured and computed values for each parameter (except Spd), presented in Figure 7, supports this conclusion.

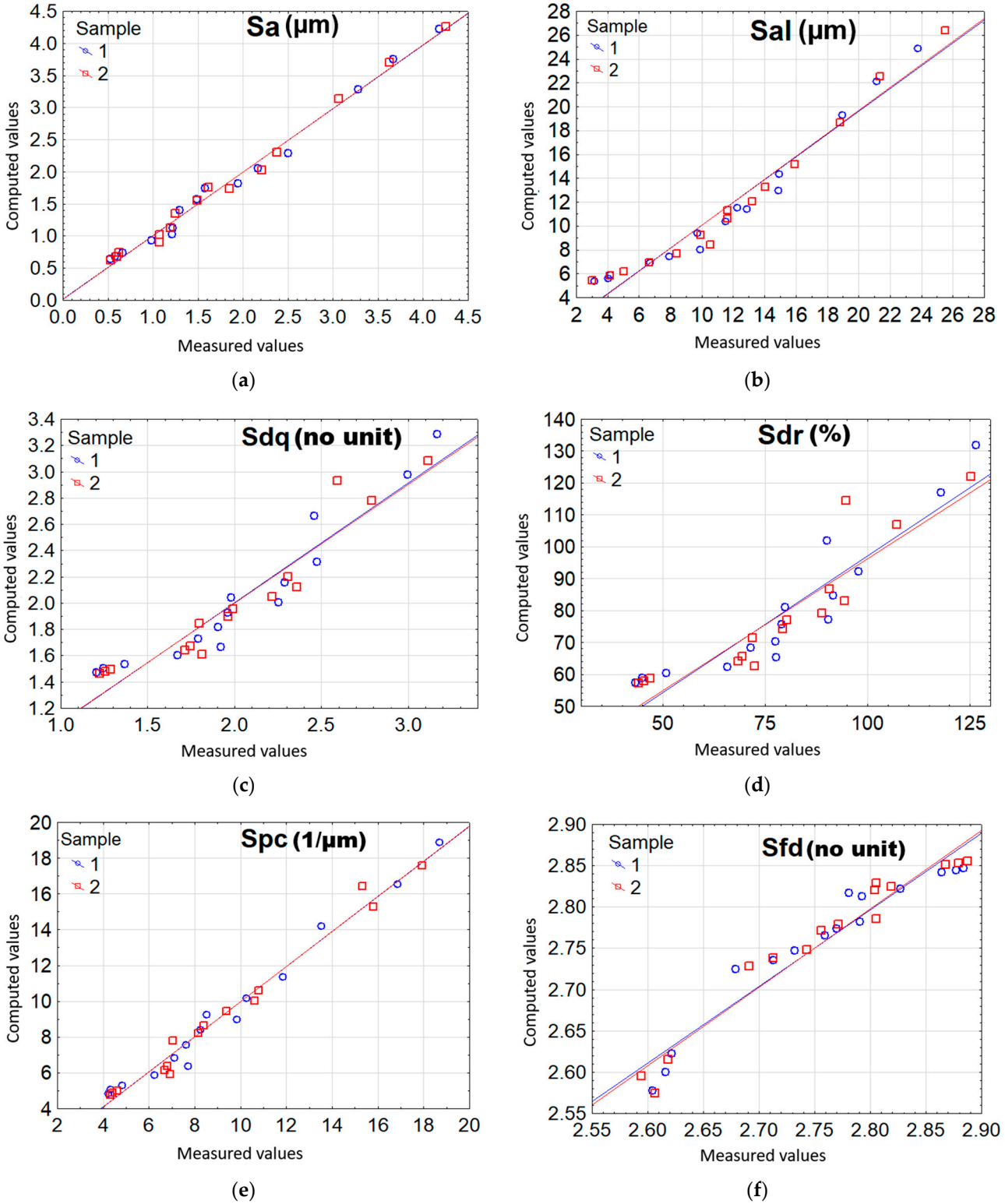


Figure 7. Graphical comparison between measured and computed values for each roughness parameter, supporting the regression model relevance and efficiency. (**a**) Sa, (**b**) Sal, (**c**) Sdq, (**d**) Sdr, (**e**) Spc, and (**f**) Sfd.

For the Spd parameter, which represents the number of peaks per unit area, it is more appropriate to adopt a nonlinear model formulated as follows:

$$Spd = (a + b.D + d.D.P)^2 \quad (5)$$

This formulation better captures the physical nature of this parameter. A comparison between the linear and nonlinear models for Spd shows that the nonlinear model achieves a higher coefficient of determination (R^2 = 0.90, CI = [0.81, 0.96]) compared to the linear model (R^2 = 0.77, CI = [0.70, 0.84]), as it can be seen on Figure 8. This demonstrates that the nonlinear model is better suited to describe the variation in Spd as a function of the blasting conditions. The graphical comparison between measured and computed values for both regression model, (4) and (5) is presented, respectively, in Figures 9a and 9b.

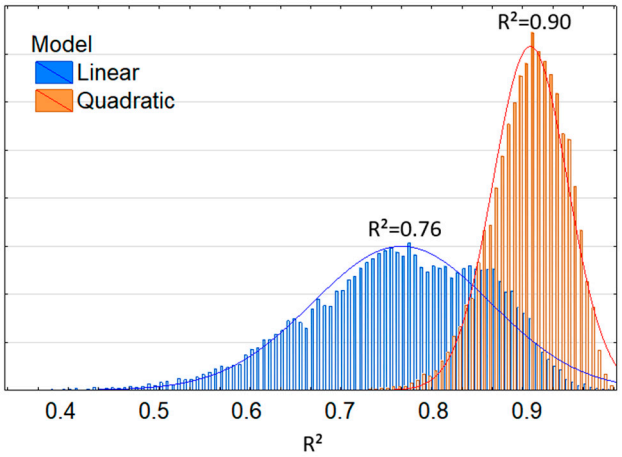
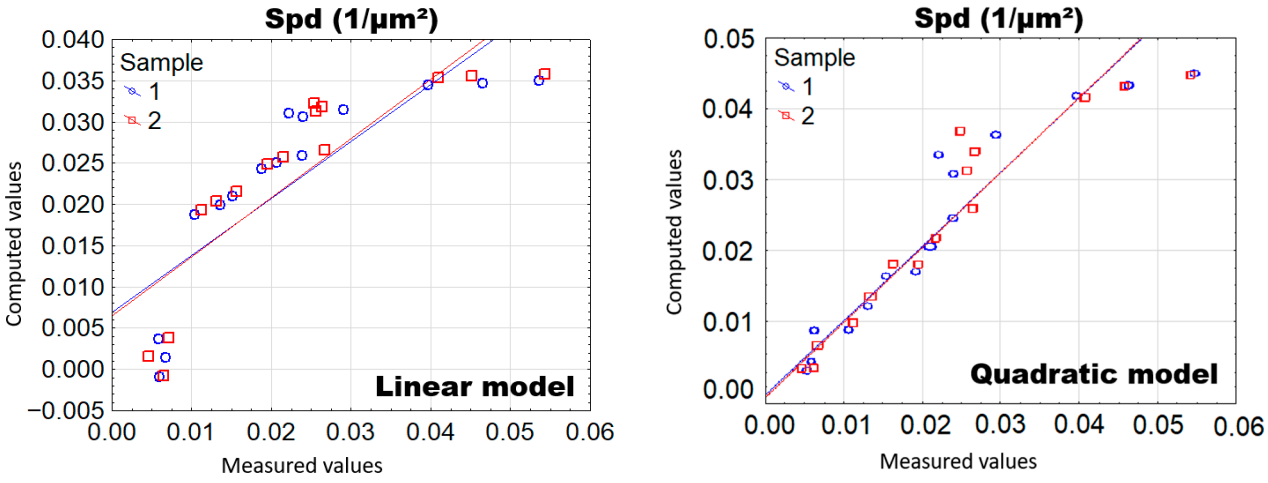


Figure 8. Statistical distributions of the coefficient of determination from the bootstrap analysis from each regression model used to fit the Spd parameter. The comparison between the linear and nonlinear models shows that the nonlinear model achieves a higher coefficient of determination compared to the linear model.



(**a**) (**b**)

Figure 9. Graphical comparison between measured and computed values for (**a**) linear and (**b**) quadratic regression models. The nonlinear model (quadratic) achieves a better fit compared to the linear model.

5. Physics Origin of the Sa Model

5.1. Modeling

To justify the model expressing Sa as a function of the abrasive particle size distribution D and the pressure P, it is necessary to describe the physical mechanism by which a grain impact modifies the surface. For this purpose, the kinetic energy E of a grain with diameter D and material density ρ, accelerated by the sandblasting pressure P, is therefore considered (6).

$$E = \rho \pi D^3 P/6 \tag{6}$$

In case of plastic indentation, the applied force F is proportional to the contact area Σ and the material hardness H. Considering that corundum grains exhibit sharp geometries; their impact can be approximated as a conical indentation, which implies that the force is proportional to the square of the penetration depth u (7). The corresponding indentation energy can therefore be expressed by (8).

$$F = H\Sigma \rightarrow F \propto Hu^2 \tag{7}$$

$$E = \int_0^u F du\prime \approx \int_0^h Hu\prime^2 du\prime = Hu^3 \tag{8}$$

Assuming that kinetic energy is fully converted into strain energy, the penetration depth u can be expressed as a function of the grain size D and the pressure P:

$$u = (E/H)^{1/3} \propto DP^{1/3} \tag{9}$$

This relation indicates that the average deformation height—corresponding to the Sa—increases with both particle diameter and applied pressure, in agreement with physical intuition. Consequently, the following relation can be established:

$$Sa = kDP^{\frac{1}{3}} \tag{10}$$

where k is a proportionality constant encompassing material properties (hardness, elasticity) and experimental factors such as particles shape. Physically, this means that larger particles and higher pressures produce deeper indentations, leading to greater mean surface roughness.

Examination of the experimental results indicates that, for a given grit size, the effect of pressure on surface roughness is relatively weak. Thus, by performing a first-order linearization of (9) around arbitrary reference values D_0 and P_0 within the experimental range, it yields:

$$Sa = k\frac{2}{3}P_0^{1/3}D + k\frac{1}{3}P_0^{-2/3}DP \tag{11}$$

or equivalently:

$$Sa = a + b.D + d.D.P \tag{12}$$

where a = 0, b = $(2/3)kP_0{}^{1/3}$, and d = $(1/3)kP_0{}^{-2/3}$. Note that a similar conclusion is obtained when assuming a spherical indentation model, although the numerical values of the coefficients differ.

The coefficient b multiplies D and reflects the linear effect of particle diameter on Sa, and the coefficient d multiplies the coupled term DP, representing the combined effect of particle diameter and pressure. No term linear in P alone appears; the only P dependent term is the coupled DP term. The coefficient a is theoretically zero, yet experimentally it takes a nonzero value. Because the present model assumes a complete conversion of kinetic energy into plastic deformation, this observed offset can be attributed to the existence of a

pressure threshold needed to overcome the surface's elastic response, thereby shifting the measured roughness values.

This linear-bilinear formulation is physically consistent with the principles of particles kinetic energy and material plasticity and remains valid within the studied experimental range, reproducing more than 95% of the observed variation in Sa. At higher pressures or much larger particles, additional nonlinear effects may become significant.

5.2. Validation Protocol

To validate the simplification of the mean surface roughness Sa as a bilinear function of sandblasting parameters D (particle diameter) and P (pressure), derived from the physical assumption in (9), the following protocol is applied:

1. Simulation of Surface Roughness Data: Define a proportionality constant (k = 0.01). Simulate Sa for all combinations of particle diameters (D = 25, 50, 90, 125, 250) and pressures (P = 2, 3, 4). Compute Sa using (9).
2. Bilinear Regression: Fit a bilinear model to the simulated data using Equation (12) (Figure 10). Estimate the coefficients a, b and d using nonlinear regression software (Table 5). Here, a represents a possible measurement offset due to the elastic barrier that must be overcome before a plastic action can be exerted on the surface. b captures the effect of particle size, and d accounts for the coupled influence of particle size and pressure.
3. Validation of the Approximation: Compare predicted values from the bilinear model with the simulated ones (Figure 11). The relative errors between the predicted and simulated Sa values were very small, ranging from approximately (−0.0049) to (0.0086), with a mean close to zero (0.0064) and a standard deviation of 0.0086. This confirms that the bilinear model accurately reproduces the physically based simulated roughness across the experimental ranges of particle size and pressure.
4. Interpretation: A small error confirms that the bilinear model sufficiently captures the dependency of Sa on D and P within the experimental range.

Table 5. Fitted parameters of the bilinear model. The results indicate that the intercept a is statistically negligible, while coefficients b and d are highly significant, confirming that surface roughness scales predominantly with particle size D and with the combined term DP, as predicted by the physical model.

	Value	SD	95% CI
a	1.40×10^{-5}	5.70×10^{-3}	$[-12.5 \times 10^{-3}\ 12.5 \times 10^{-3}]$
b	9.39×10^{-3}	1.02×10^{-4}	$[9.16 \times 10^{-3}\ 9.61 \times 10^{-3}]$
d	1.64×10^{-3}	3.10×10^{-5}	$[1.57 \times 10^{-3}\ 1.70 \times 10^{-3}]$

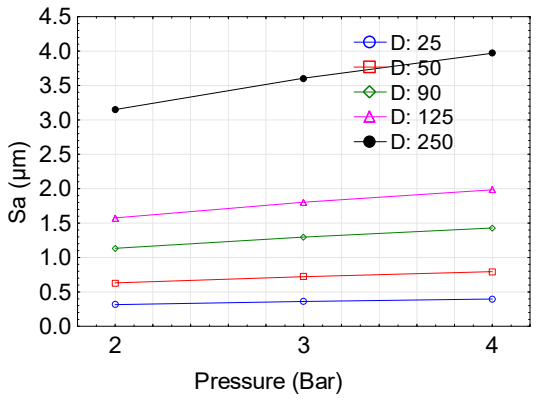


Figure 10. Linear-fitted evolution of the mean surface roughness (Sa) as a function of blasting pressure P for different particle diameters D.

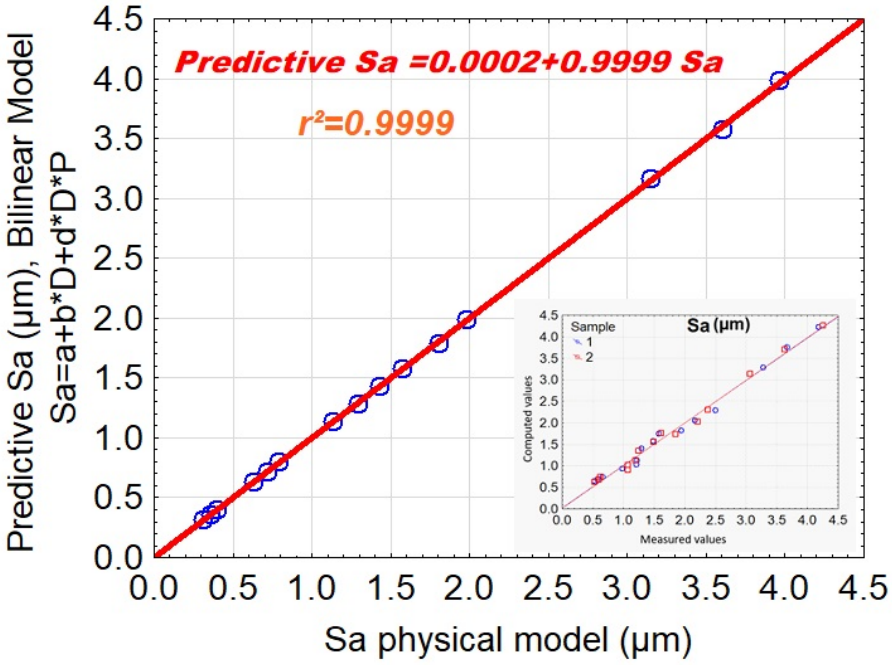


Figure 11. Comparison between simulated (physical model) and predicted (bilinear model) values of mean surface roughness (physical model). The data points closely follow the identity line (slope = 0.9999, intercept = 0.0002) confirming the strong agreement between the physical model and its bilinear approximation.

6. Conclusions and Perspectives

This work deals with a comprehensive methodology to characterize the roughness of sandblasted surfaces by combining precise 3D measurements with robust statistical approaches. Through the evaluation of eight standardized parameters and the systematic application of the ANOVA method, regression modeling, and bootstrap-based uncertainty estimation, it was possible to identify the descriptors most sensitive to blasting conditions and to establish predictive laws linking grit size, pressure, and surface texture. The introduction of a nonlinear model for the density of peaks (Spd) further underlines the capacity of the approach to adapt to the intrinsic complexity of certain roughness parameters.

The results obtained highlight the predominant role of abrasive particle size and its interaction with pressure, providing a quantitative basis for understanding the physical mechanisms that govern surface texturing. The methodology also demonstrates that a simplified—but statistically validated—modeling can retain predictive accuracy while remaining interpretable.

From an application perspective, this work opens the way to controlled preparation of surfaces adapted to specific functional objectives such as adhesion, wettability, or fatigue resistance. By offering predictive tools directly connected to process parameters, the methodology paves the way for optimized industrial sandblasting protocols, enabling both reproducibility and customization of surface states. Future perspectives include extending the approach to other classes of materials, integrating additional descriptors such as chemical or crystallographic surface modifications, and coupling the present models with numerical simulations of particle–surface interactions. Such developments would further enhance the capacity to design surfaces with tailored functionalities, and therefore represent an attractive opportunity for industrial partners seeking efficient and reliable surface engineering strategies.

From an industrial transfer perspective, the proposed approach offers a practical and reliable pathway to controlled surface preparation. By directly linking sandblasting

parameters to targeted surface properties, it enables reproducible protocols tailored to adhesion, wettability, or fatigue performance requirements. This predictive capability opens perspectives to optimize blasting processes, reduce variability, and accelerate the development of functionalized surfaces adapted to specific application domains.

Author Contributions: Conceptualization, M.B.; methodology, E.C.; software, J.L. and F.R.; validation, R.D.; formal analysis, R.V.; investigation, I.P.-S.; data curation, N.Z.; writing—original draft preparation, E.C. and M.B.; writing—review and editing, E.C. and M.B.; supervision, K.A.; project administration, S.B. All authors have read and agreed to the published version of the manuscript.

Funding: The authors thank the ANR agency for the funding of this work, included in the "Must^{implant}" project (ANR-22-CE51-0031).

Data Availability Statement: Data are contained within the article.

Conflicts of Interest: The authors declare no conflicts of interest.

Appendix A

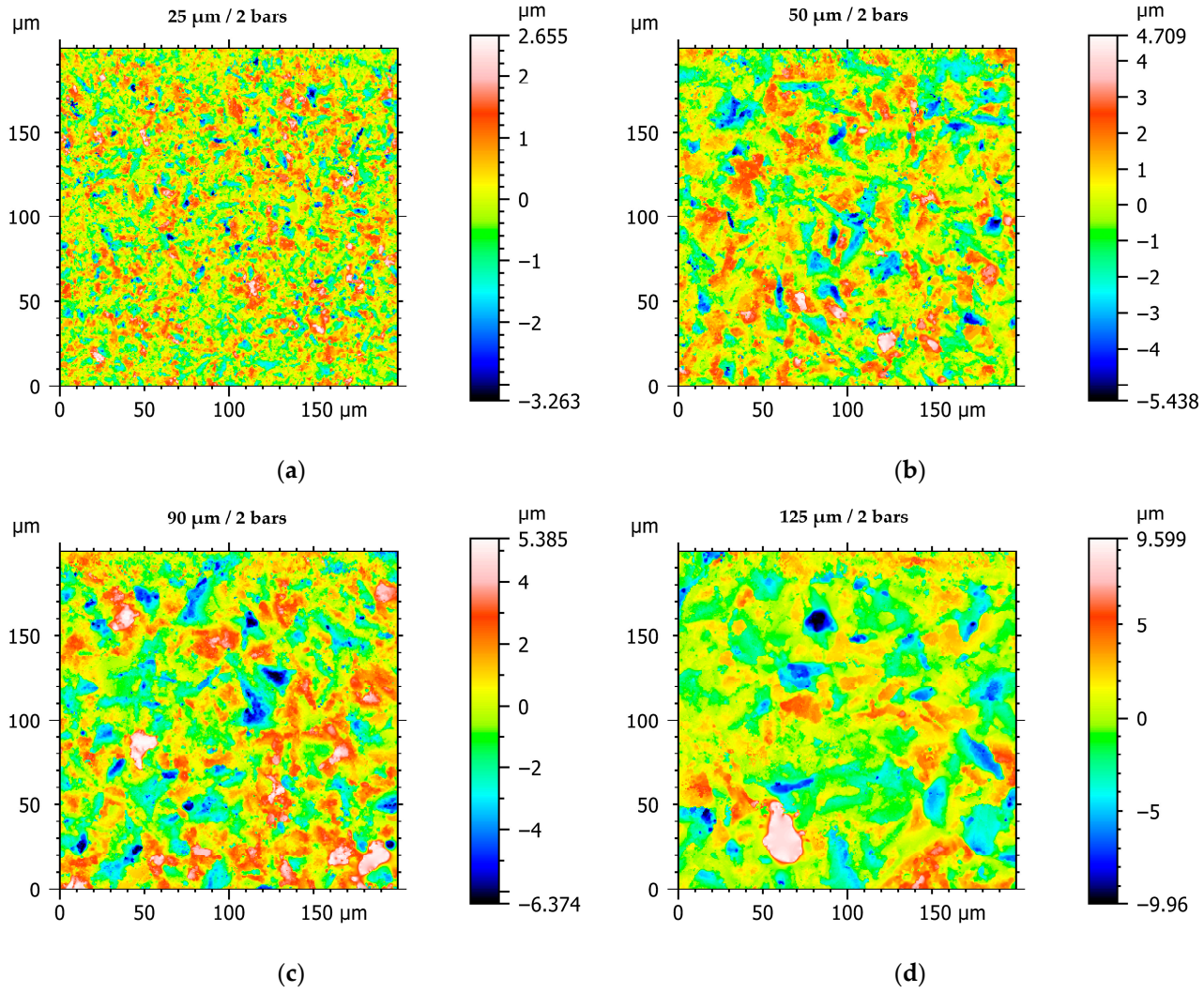
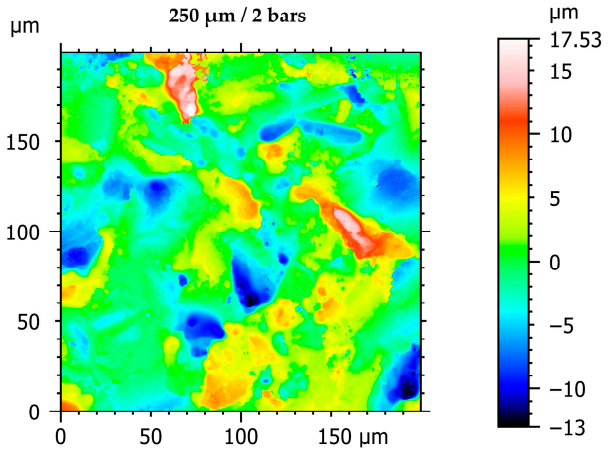
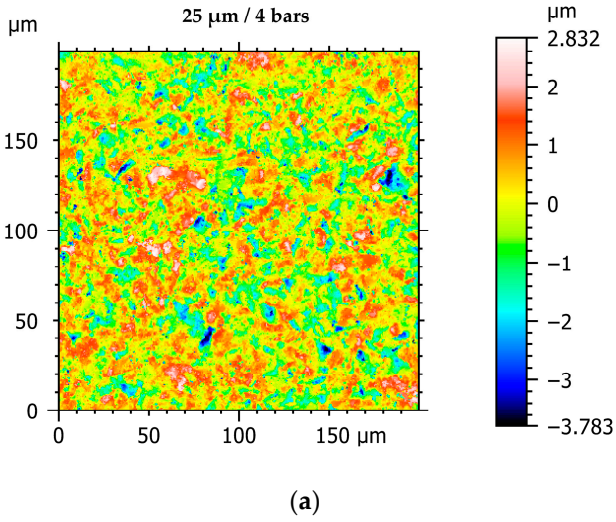


Figure A1. *Cont.*

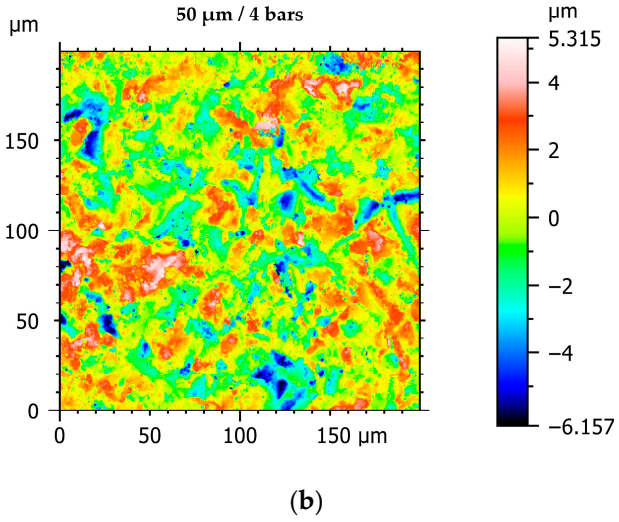


(**e**)

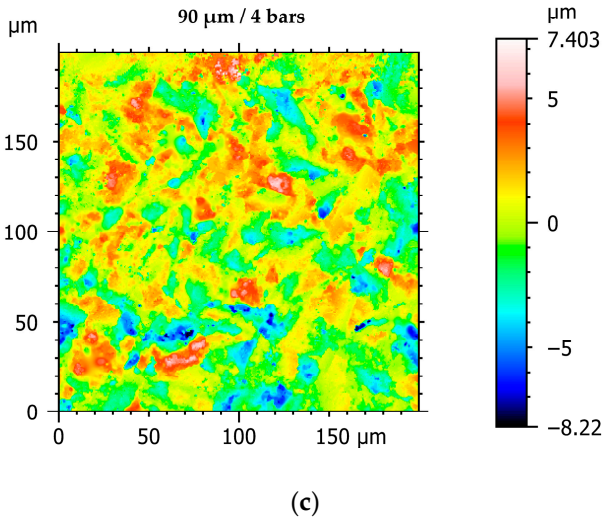
Figure A1. Representative surfaces obtained for a grit size of (**a**) 25 µm, (**b**) 50 µm, (**c**) 90 µm, (**d**) 125 µm and (**e**) 250 µm, at a pressure of 2 bars.



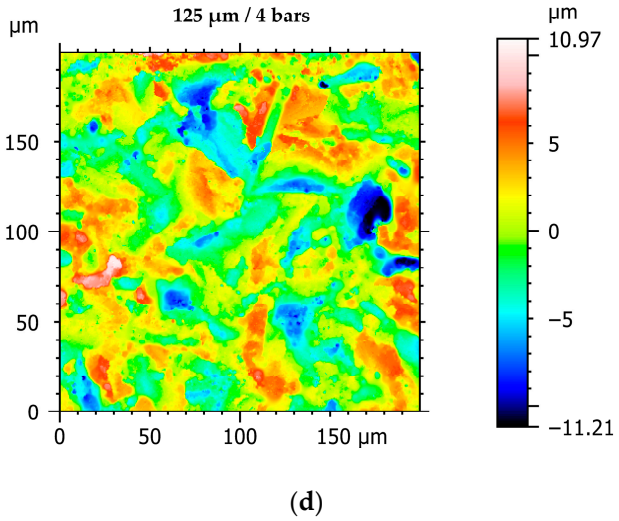
(**a**)



(**b**)

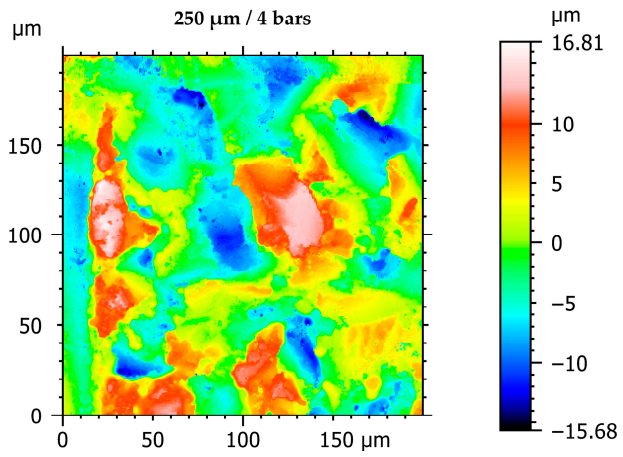


(**c**)



(**d**)

Figure A2. *Cont.*



(**e**)

Figure A2. Representative s. faces obtained for a grit size of (**a**) 25 µm, (**b**) 50 µm, (**c**) 90 µm, (**d**) 125 µm and (**e**) 250 µm, at a pressure of 4 bars.

Appendix B

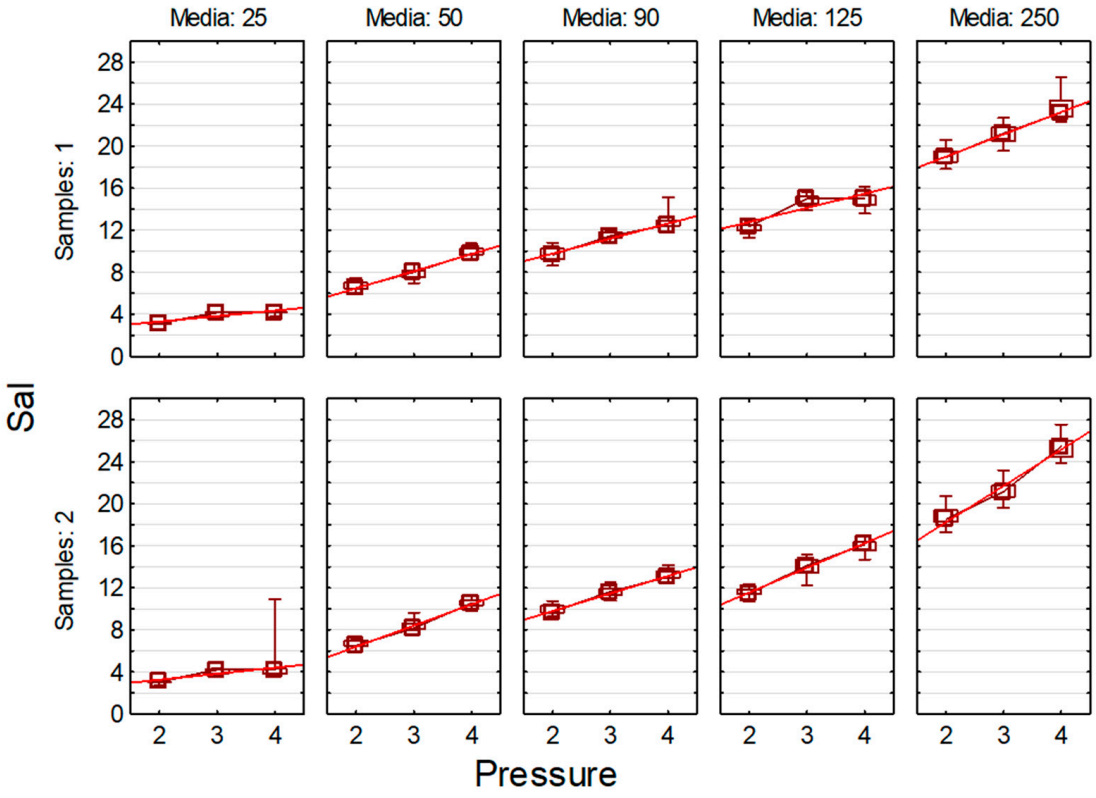


Figure A3. Evolution of the Sal (µm) according to the pressure (bar) and the grit size (µm). The box plots show the statistical parameters, respectively, the 1st and 9th decile and the 1st, 2nd and 3rd quartile, obtained from 60 measured images.

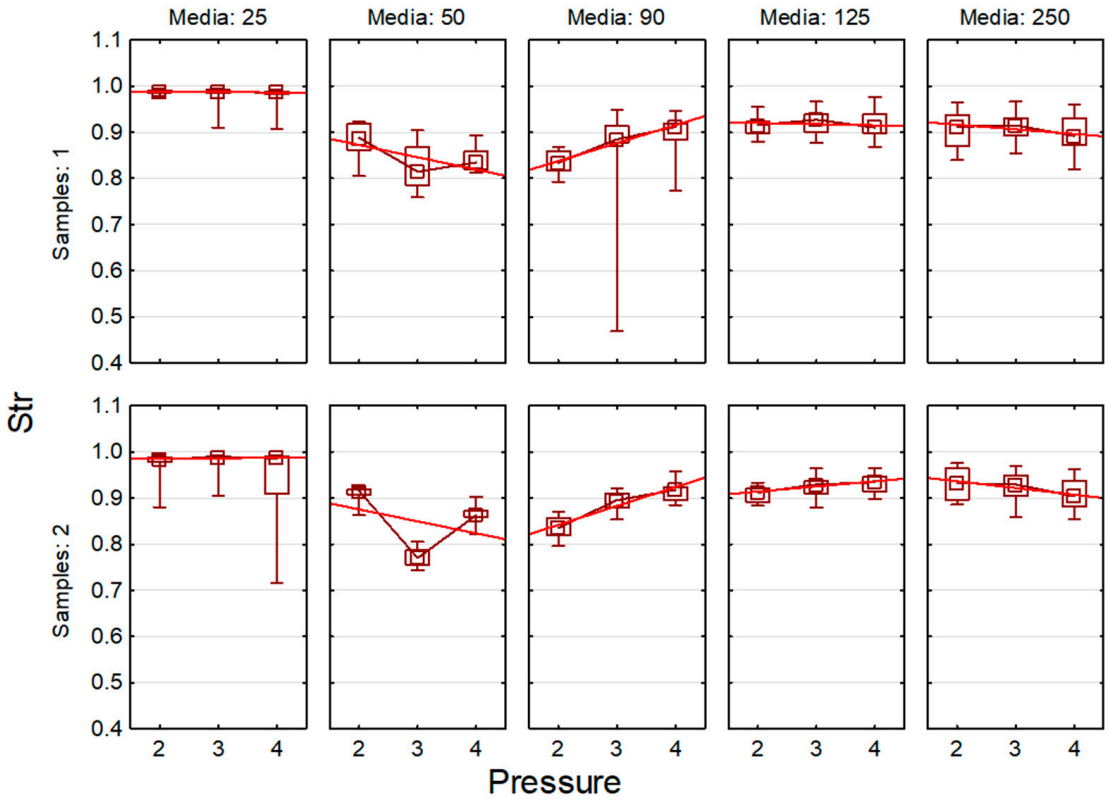


Figure A4. Evolution of the Str (no unit) according to the pressure (bar) and the grit size (µm). The box plots show the statistical parameters, respectively, the 1st and 9th decile and the 1st, 2nd and 3rd quartile, obtained from 60 measured images.

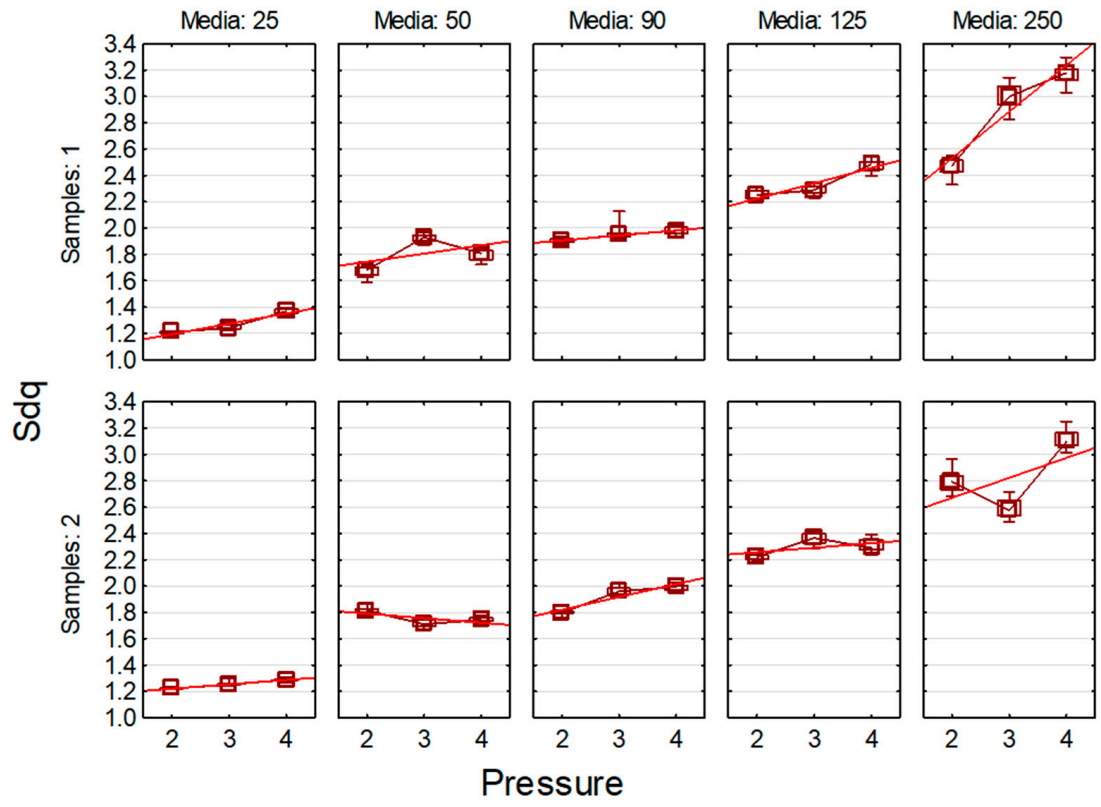


Figure A5. Evolution of the Sdq (no unit) according to the pressure (bar) and the grit size (µm). The box plots show the statistical parameters, respectively, the 1st and 9th decile and the 1st, 2nd and 3rd quartile, obtained from 60 measured images.

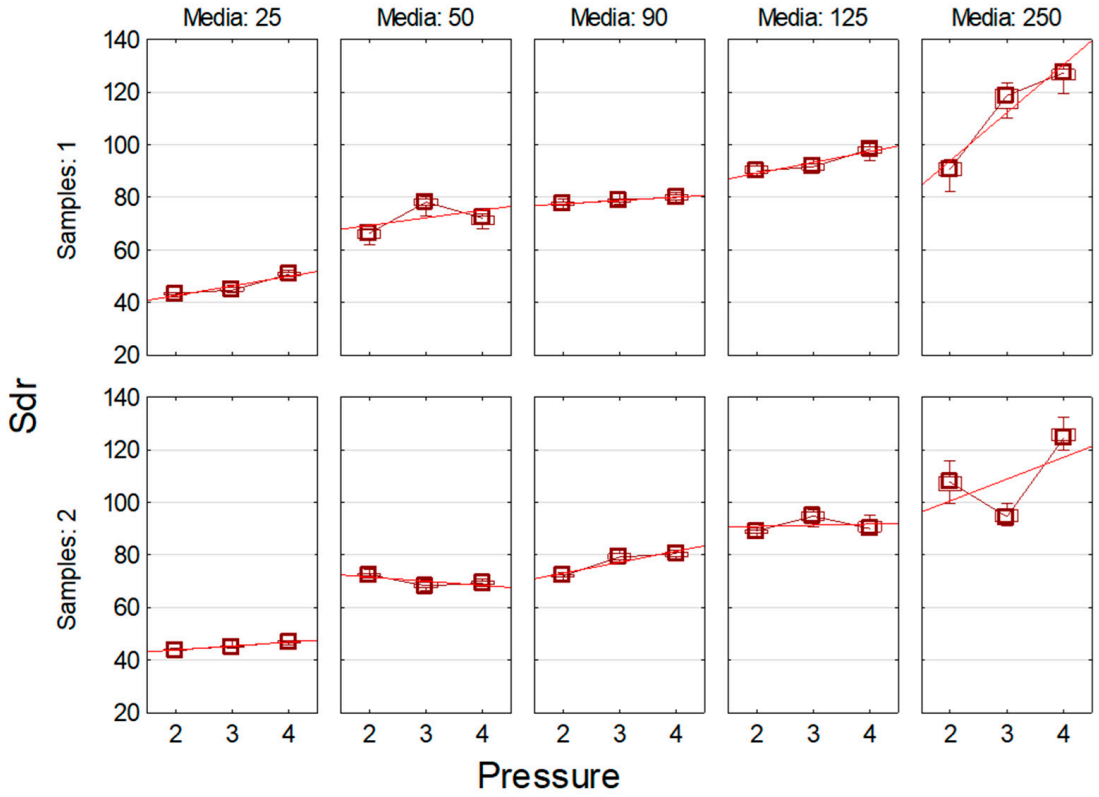


Figure A6. Evolution of the Sdr (%) according to the pressure (bar) and the grit size (µm). The box plots show the statistical parameters, respectively, the 1st and 9th decile and the 1st, 2nd and 3rd quartile, obtained from 60 measured images.

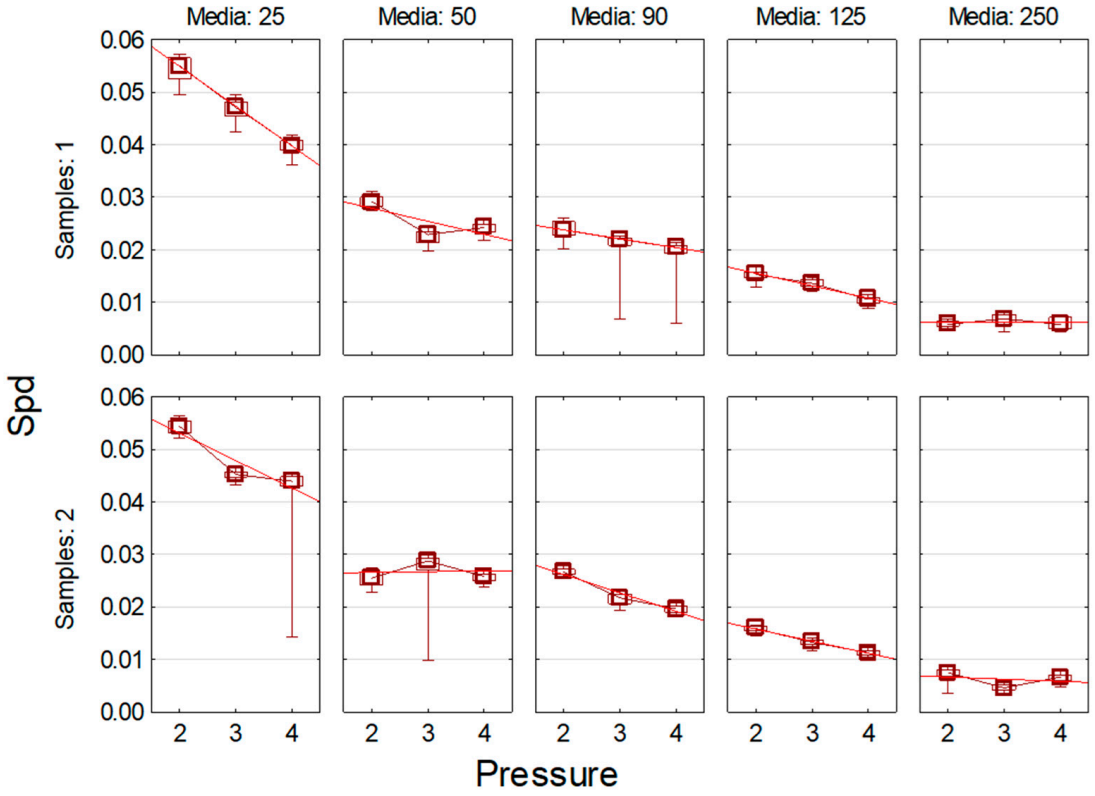


Figure A7. Evolution of the Spd ($1/\mu m^2$) according to the pressure (bar) and the grit size (µm). The box plots show the statistical parameters, respectively, the 1st and 9th decile and the 1st, 2nd and 3rd quartile, obtained from 60 measured images.

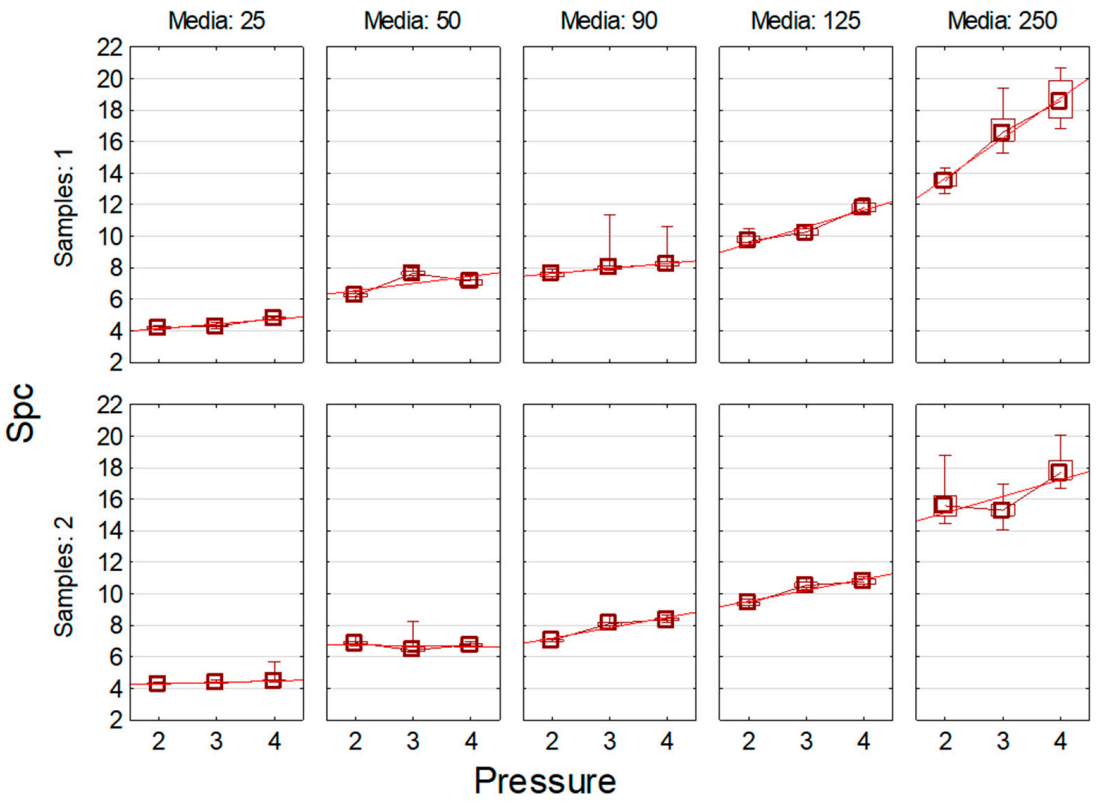


Figure A8. Evolution of the Spc (1/µm) according to the pressure (bar) and the grit size (µm). The box plots show the statistical parameters, respectively, the 1st and 9th decile and the 1st, 2nd and 3rd quartile, obtained from 60 measured images.

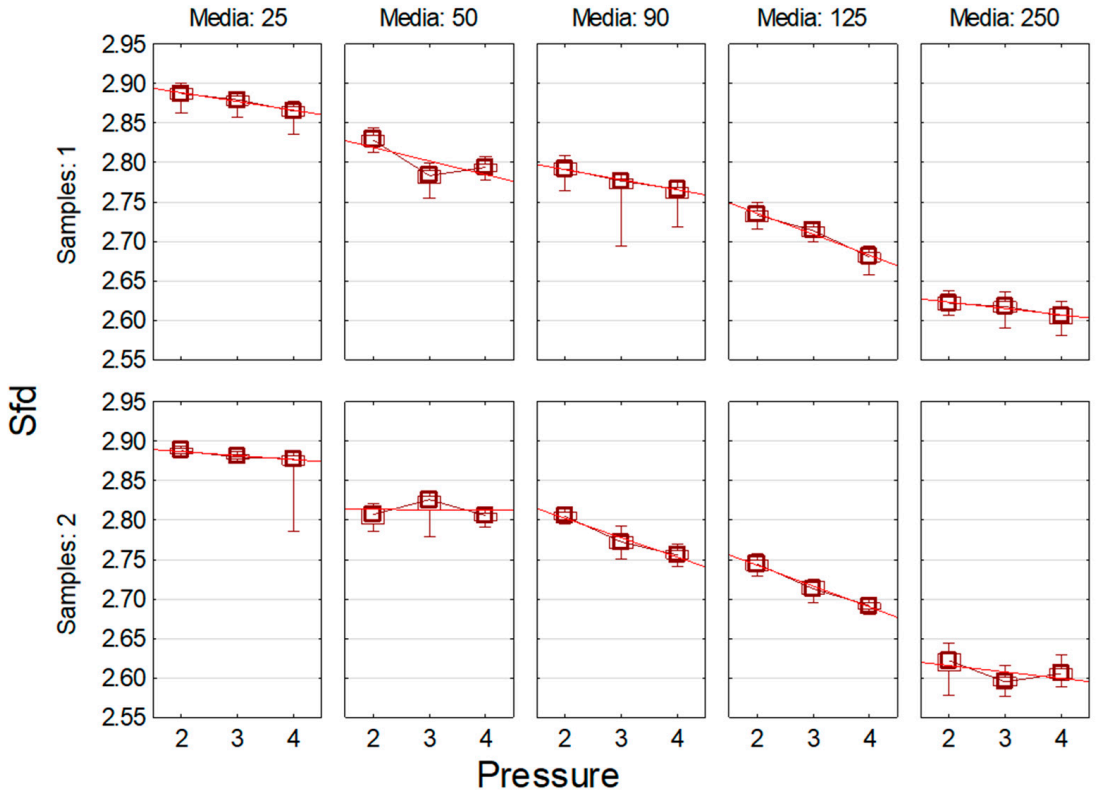


Figure A9. Evolution of the Sfd (no unit) according to the pressure (bar) and the grit size (µm). The box plots show the statistical parameters, respectively, the 1st and 9th decile and the 1st, 2nd and 3rd quartile, obtained from 60 measured images.

Appendix C

Appendix C.1 Paired Data Bootstrap Method

Here is how the paired bootstrap is implemented in a general practice:

Original Dataset—Start with the original dataset consisting of N pairs of data points $(X_1\ Y_1)$, $(X_2\ Y_2)$,$\cdots$, $(X_N\ Y_N)$ where X_i is a variable and Y_i its corresponding image;

Generating Bootstrap Samples—Randomly samples N pairs from the original dataset *with replacement*. This means that some pairs may be selected multiple times while others may not be selected at all. Each resampled set of N pairs constitutes a single bootstrap sample;

Fitting the Model—For each bootstrap sample, the fitting model is applied, yielding to a new set of parameters;

Repeating the Process—Repeat the resampling and fitting process a large number of times (typically thousands of iterations), each iteration providing a new estimate of the model parameters.

Analyzing the Results—After completing all iterations, the distribution of the parameter estimates obtained from all the bootstrap samples are analyzed. The spread of these distributions gives us confidence intervals for each parameter, indicating the uncertainty associated with our estimates.

Appendix C.2 Residuals Bootstrap Method

Residuals bootstrap is also a resampling technique estimating the uncertainty of model parameters, but it assumes that the error terms in the model are identically distributed and independent. Here is how the residuals bootstrap is implemented in a general practice:

Original Dataset—Fit the N data points with a chosen model and retain the fitted values y_i and the associated residuals $\varepsilon_i = Y_i - y_i$;

Generating Bootstrap Samples—For each N pair of data points $(X_i\ Y_i)$, add a randomly resampled residual ε_j to the fitted value y_i. In other words, create synthetic response variables $Y_i^* = y_i + \varepsilon_j$ where ε_j is selected randomly from the list of the ε_i;

Fitting the Model—Refit the model using the fictitious response variables Y_i^*, and retain the quantities of interest;

Repeating the Process—Repeat the resampling and fitting process a large number of times, with each iteration providing a new estimate of the model parameters.

Analyzing the Results—After completing all iterations, the distribution of the parameter estimates obtained is analyzed, allowing us to obtain confidence intervals for each parameter.

Appendix D

Table A1. Computation of the coefficient c using the regression model defined by (1) and with the same bootstrap analysis method on the 86 roughness parameters from the standard ISO 25178. The computed values are the mean value, the minimum and maximum values and the 95% confidence interval. These results lead to conclude that the coefficient c remains consistently insignificant.

Roughness Parameter	Mean Value	Min.	Max.	95% CI		Roughness Parameter	Mean Value	Min.	Max.	95% CI	
S10z	0.284	−2.184	2.996	−1.072	1.649	Shaq	2.306	−81.21	76.77	−33.10	35.80
S5p	0.251	−2.052	2.516	−0.764	1.362	Shar	−0.025	−0.090	0.060	−0.058	0.017
S5v	0.036	−1.294	1.395	−0.586	0.748	Sharq	−0.015	−0.091	0.084	−0.049	0.029
Sa	−0.008	−0.238	0.275	−0.136	0.131	Sharx	0.724	−4.424	8.519	−1.854	4.115
Sak1	0.009	−0.035	0.058	−0.015	0.035	Shax	−78.67	−919	847.6	−507.6	369
Sak2	0.006	−0.029	0.041	−0.012	0.023	Shed	0.463	−0.793	1.449	−0.125	0.996

Table A1. *Cont.*

Roughness Parameter	Mean Value	Min.	Max.	95% CI		Roughness Parameter	Mean Value	Min.	Max.	95% CI	
Sal	0.879	−1.639	3.063	−0.402	2.114	Shedq	0.339	−1.108	1.460	−0.212	0.837
Sda	5.257	−20.77	27.75	−6.740	14.58	Shedx	1.684	−5.186	8.175	−1.694	5.053
Sdaq	8.571	−72.08	86.85	−19.09	34.78	Shff	−0.006	−0.022	0.009	−0.013	0.002
Sdarq	−0.006	−0.095	0.109	−0.057	0.056	Shffq	0.0002	−0.003	0.003	−0.001	0.002
Sdarx	−0.425	−7.258	6.743	−3.804	3.164	Shffx	−0.025	−0.166	0.099	−0.089	0.031
Sdax	65.36	−675.9	837.9	−284.9	442.3	Shh	0.034	−0.208	0.302	−0.081	0.150
Sdc	−0.007	−0.708	0.824	−0.397	0.430	Shhq	0.016	−0.090	0.130	−0.039	0.075
Sdd	0.045	−0.222	0.297	−0.089	0.179	Shhx	0.310	−1.787	1.807	−0.480	1.058
Sddq	0.027	−0.105	0.158	−0.044	0.098	Shn	−4817	−18,590	9764.7	−12,427	2743
Sddx	0.255	−1.503	1.982	−0.631	1.170	Shrn	0.001	−0.003	0.005	−0.001	0.003
Sded	0.321	−0.744	1.198	−0.189	0.756	Shrnx	−0.002	−0.025	0.022	−0.014	0.011
Sdedq	0.301	−0.925	1.406	−0.212	0.724	Shv	0.597	−15.83	12.34	−4.797	5.753
Sdedx	2.045	−4.253	8.685	−1.196	5.191	Shvq	−2.490	−68.43	62.46	−29.06	24.40
Sdff	−0.005	−0.019	0.010	−0.012	0.002	Shvx	−106.9	−2330	2363	−925.7	723.4
Sdffq	0.0004	−0.002	0.003	−0.001	0.002	Sk	−0.103	−1.022	0.894	−0.625	0.404
Sdffx	−0.032	−0.159	0.078	−0.091	0.035	Sku	0.574	−1.991	5.066	−0.353	2.260
Sdn	−4267	−19,567	10,444	−12,479	3380	Smc	0.002	−0.328	0.414	−0.187	0.210
Sdq	−0.012	−0.319	0.316	−0.187	0.164	Smr	−0.144	−0.876	0.448	−0.451	0.170
Sdr	−1.317	−18.64	15.34	−10.69	7.984	Smrk1	0.152	−1.169	1.483	−0.450	0.762
Sdrn	0.0002	−0.007	0.005	−0.003	0.003	Smrk2	−0.025	−1.095	0.733	−0.460	0.368
Sdrnq	−0.001	−0.003	0.002	−0.002	0.001	Sp	0.258	−1.86	2.869	−0.762	1.414
Sdrnx	−0.006	−0.032	0.022	−0.017	0.006	Spc	−0.070	−1.279	1.251	−0.715	0.565
Sds	−0.006	−0.026	0.016	−0.018	0.006	Spd	−0.005	−0.020	0.009	−0.013	0.003
Sdv	1.215	−8.859	9.604	−3.026	4.574	Spk	0.035	−0.442	0.539	−0.201	0.269
Sdvq	5.709	−66.43	57.87	−20.55	27.18	Spkx	0.308	−1.732	2.826	−0.767	1.552
Sdvx	160.9	−2060	2272	−800.1	1004	Sq	0.002	−0.263	0.335	−0.148	0.171
Sfd	−0.015	−0.058	0.024	−0.039	0.007	Ssc	−0.052	−0.661	0.653	−0.398	0.294
Sha	6.625	−31.67	40.09	−9.138	19.74	Ssk	0.078	−0.234	0.448	−0.055	0.228
Roughness parameter	Mean Value	Min.	Max.	95% CI							
Ssw	−3.623	−16.92	13.04	−10.65	4.184						
St	0.282	−2.638	3.032	−1.067	1.663						
Std	1.244	−18.59	21.42	−7.598	10.82						
Str	−0.002	−0.106	0.137	−0.054	0.050						
Sv	0.035	−1.180	1.579	−0.591	0.745						
Svc	−0.009	−1.855	1.815	−0.912	0.899						
Svd	−0.004	−0.020	0.011	−0.012	0.004						
Svk	0.031	−0.424	0.525	−0.184	0.260						
Svkx	0.086	−0.989	1.245	−0.416	0.600						
Sz	0.287	−2.650	3.087	−1.055	1.652						
Vm	0.002	−0.02	0.023	−0.010	0.013						
Vmc	−0.016	−0.299	0.299	−0.171	0.148						
Vmp	0.002	−0.022	0.026	−0.010	0.013						
Vv	0.004	−0.349	0.389	−0.187	0.218						
Vvc	0.0003	−0.330	0.399	−0.171	0.192						
Vvv	0.002	−0.040	0.046	−0.020	0.026						

References

1. Tawade, P.; Shembale, S.; Hussain, S.; Sabiruddin, K. Effects of Different Grit Blasting Environments on the Prepared Steel Surface. *J. Therm. Spray Technol.* **2023**, *32*, 1535–1553. [CrossRef]
2. Zhang, Z.; Shen, Z.; Wu, H.; Li, L.; Fu, X. Study on Preparation of Superhydrophobic Ni-Co Coating and Corrosion Resistance by Sandblasting–Electrodeposition. *Coatings* **2020**, *10*, 1164. [CrossRef]
3. Wang, J.; Ai, C.; Yun, X.; Chen, Z.; He, B. Effects of 3D Roughness Parameters of Sandblasted Surface on Bond Strength of HVOF Sprayed WC-12Co Coatings. *Coatings* **2022**, *12*, 1451. [CrossRef]
4. Deng, H.; Xu, K.; Liu, S.; Zhang, C.; Zhu, X.; Zhou, H.; Xia, C.; Shi, C. Impact of Engineering Surface Treatment on Surface Properties of Biomedical TC4 Alloys under a Simulated Human Environment. *Coatings* **2022**, *12*, 157. [CrossRef]
5. Zhou, X.; Kang, M.; Liu, J.; Lin, J.; Ndumia, J.N.; Yang, J. Effect of Grit-Blasting Pretreatment on the Bond Strength of Arc-Sprayed Fe-Based Coating. *JOM* **2023**, *75*, 3268–3276. [CrossRef]
6. Miturska-Barańska, I.; Rudawska, A.; Doluk, E. The Influence of Sandblasting Process Parameters of Aerospace Aluminium Alloy Sheets on Adhesive Joints Strength. *Materials* **2021**, *14*, 6626. [CrossRef]
7. Paul, B.; Hofmann, A.; Weinert, S.; Frank, F.; Wolff, U.; Krautz, M.; Edelmann, J.; Gee, M.W.; Reeps, C.; Hufenbach, J. Effect of Blasting Treatments on the Surface Topography and Cell Adhesion on Biodegradable FeMn-Based Stents Processed by Laser Powder Bed Fusion. *Adv. Eng. Mater.* **2022**, *24*, 2200961. [CrossRef]
8. Faadhila, A.; Taufiqurrakhman, M.; Katili, P.A.; Rahman, S.F.; Lestari, D.C.; Whulanza, Y. Optimizing PEEK implant surfaces for improved stability and biocompatibility through sandblasting and the platinum coating approach. *Front. Mech. Eng.* **2024**, *10*, 1360743. [CrossRef]
9. Al Qahtani, W.; Schille, C.; Spintzyk, S.; Al Qahtani, M.; Engel, E.; Geis-Gerstorfer, J.; Rupp, F.; Scheideler, L. Effect of surface modification of zirconia on cell adhesion, metabolic activity and proliferation of human osteoblasts. *Biomed. Eng./Biomed. Tech.* **2017**, *62*, 75–87. [CrossRef]
10. Stoilov, M.; Stoilov, L.; Enkling, N.; Stark, H.; Winter, J.; Marder, M.; Kraus, D. Effects of Different Titanium Surface Treatments on Adhesion, Proliferation and Differentiation of Bone Cells: An In Vitro Study. *J. Funct. Biomater.* **2022**, *13*, 143. [CrossRef] [PubMed]
11. Liu, C.F.; Chang, K.C.; Sun, Y.S.; Nguyen, D.T.; Huang, H.H. Combining Sandblasting, Alkaline Etching, and Collagen Immobilization to Promote Cell Growth on Biomedical Titanium Implants. *Polymers* **2021**, *13*, 2550. [CrossRef]
12. Fraulob, M.; Vayron, R.; Le Cann, S.; Lecuelle, B.; Hérivaux, Y.; Albini Lomami, H.; Flouzat Lachaniette, C.H.; Haïat, G. Quantitative ultrasound assessment of the influence of roughness and healing time on osseointegration phenomena. *Sci. Rep.* **2020**, *10*, 21962. [CrossRef]
13. Shaaban, S.; Bekheet, S.; Abdallah, S.; Mahmoud, T. Effect of Sandblasting Surface Treatment on the Bond Strength and Surface Roughness between the 3D-Printed Denture Base and Silicon-Based Soft Liner. *Egypt. Dent. J.* **2023**, *69*, 2175–2184. [CrossRef]
14. Ciobotaru, I.A.; Stoicanescu, M.; Budei, R.; Cojocaru, A.; Vaireanu, D.-I. Considerations Regarding Sandblasting of Ti and Ti6Al4V Used in Dental Implants and Abutments as a Preconditioning Stage for Restorative Dentistry Works. *Appl. Sci.* **2024**, *14*, 7365. [CrossRef]
15. Osak, P.; Maszybrocka, J.; Zubko, M.; Rak, J.; Bogunia, S.; Łosiewicz, B. Influence of Sandblasting Process on Tribological Properties of Titanium Grade 4 in Artificial Saliva for Dentistry Applications. *Materials* **2021**, *14*, 7536. [CrossRef] [PubMed]
16. Zhixin, W.; Xian, R.; Lei, Z.; Xueyang, X.; Hui, M. Effects of Substrate Surface Characteristics on the Adhesion Properties of Geopolymer Coatings. *ACS Omega* **2022**, *7*, 11988–11994. [CrossRef]
17. Nonnenmann, T.; Beygi, R.; Carbas, R.J.C.; da Silva, L.F.; Öchsner, A. Synergetic effect of adhesive bonding and welding on fracture load in hybrid joints. *J. Adv. Join. Process.* **2022**, *6*, 100122. [CrossRef]
18. Tan, B.; Hu, Y.; Yuan, B.; Hu, X.; Huang, Z. Optimizing adhesive bonding between CFRP and Al alloy substrate through resin pre-coating by filling micro-cavities from sandblasting. *Int. J. Adhes. Adhes.* **2021**, *110*, 102952. [CrossRef]
19. Kido, D.; Komatsu, K.; Suzumura, T.; Matsuura, T.; Cheng, J.; Kim, J.; Park, W.; Ogawa, T. Influence of Surface Contaminants and Hydrocarbon Pellicle on the Results of Wettability Measurements of Titanium. *Int. J. Mol. Sci.* **2023**, *24*, 14688. [CrossRef]
20. Lillemäe-Avi, I.; Liinalampi, S.; Lehtimäki, E.; Remes, H.; Lehto, P.; Romanoff, J.; Ehlers, S.; Niemelä, A. Fatigue strength of high-strength steel after shipyard production process of plasma cutting, grinding, and sandblasting. *Weld World* **2018**, *62*, 1273–1284. [CrossRef]
21. Lara, A.; Roca, M.; Parareda, S.; Cuadrado, N.; Calvo, J.; Casellas, D. Effect of Sandblasting on Low and High-Cycle Fatigue Behaviour after Mechanical Cutting of a Twinning-Induced Plasticity Steel. *MATEC Web Conf.* **2018**, *165*, 18002. [CrossRef]
22. Sun, X.D.; Liu, T.T.; Wang, Q.Q.; Zhang, J.; Cao, M.S. Surface Modification and Functionalities for Titanium Dental Implants. *ACS Biomater. Sci. Eng.* **2023**, *9*, 4442–4461. [CrossRef]
23. Wennerberg, A.; Albrektsson, T. Effects of titanium surface topography on bone integration: A systematic review. *Clin. Oral Implant. Res.* **2009**, *20* (Suppl. 4), 172–184. [CrossRef]
24. Ogawa, T.; Hirota, M.; Shibata, R.; Matsuura, T.; Komatsu, K.; Saruta, J.; Att, W. The 3D theory of osseointegration: Material, topography, and time as interdependent determinants of bone-implant integration. *Int. J. Implant Dent.* **2025**, *11*, 49. [CrossRef]

25. Ho, H.S.; Bigerelle, M.; Vincent, R.; Deltombe, R. Correlation modeling between process condition of sandblasting and surface texture: A multi-scale approach. *Scanning* **2016**, *38*, 191–201. [CrossRef]
26. As'ad, M.; Febriantoko, B.W.; Riyadi, T.W.B.; Pahlevi, R.F. The Influence of Air Pressure on Surface Roughness Values in the Sandblasting Process of ST-37 Steel Plates. *Eng. Proc.* **2024**, *63*, 28. [CrossRef]
27. Aldio, R.Z.; Dedikarni; Saputra, B. Effect of Spraying and Mesh Size on Surface Roughness of SS400 Steel Sandblasting Process. *J. Renew. Energy Mech.* **2021**, *4*, 63–75. [CrossRef]
28. Queiroz, J.R.; Botelho, M.A.; Sousa, S.A.; Martinelli, A.E.; Özcan, M. Evaluation of spatial and functional roughness parameters on air-abraded zirconia as a function of particle type and deposition pressure. *J. Adhes. Dent.* **2015**, *17*, 77–80. [CrossRef]
29. Coskun, M.E.; Akar, T.; Tugut, F. Airborne-particle abrasion; searching the right parameter. *J. Dent. Sci.* **2018**, *13*, 293–300. [CrossRef]
30. Czepułkowska, W.; Wołowiec-Korecka, E.; Klimek, L. The Condition of Ni-Cr Alloy Surface After Abrasive Blasting with Various Parameters. *J. Mater. Eng. Perform.* **2020**, *29*, 1439–1444. [CrossRef]
31. Available online: https://www.iso.org/fr/standard/74591.html (accessed on 1 September 2025).
32. Canabarro, A.; Figueiredo, F.; Paciornik, S.; De-Deus, G. Two- and three-dimensional profilometer assessments to determine titanium roughness. *Scanning* **2009**, *31*, 174–179. [CrossRef] [PubMed]
33. Adhitya, K.; Mustika, T.; Manawan, M.; Ulfah, I.M.; Hanafi, R.; Setyadi, I.; Suryadi; Hidayat, A.; Sah, J.; Wibisono, M.; et al. Optimizing surface properties in pure titanium for dental implants: A crystallographic analysis of sandblasting and acid-etching techniques. *Powder Diffr.* **2024**, *39*, 206–216. [CrossRef]
34. Efron, B. Bootstrap Methods: Another Look at the Jackknife. *Ann. Statist.* **1979**, *7*, 1–26. [CrossRef]
35. Efron, B. Better Bootstrap Confidence Intervals. *J. Am. Stat. Assoc.* **1987**, *82*, 171–185. [CrossRef]
36. Available online: https://d2ykdomew87jzd.cloudfront.net/data-sheets/TI-6AL-4V-UNS-R56400.pdf (accessed on 1 September 2025).
37. Available online: https://www.renfert.com/fr-fr/content/download/16902/file/216640.pdf (accessed on 1 September 2025).

Disclaimer/Publisher's Note: The statements, opinions and data contained in all publications are solely those of the individual author(s) and contributor(s) and not of MDPI and/or the editor(s). MDPI and/or the editor(s) disclaim responsibility for any injury to people or property resulting from any ideas, methods, instructions or products referred to in the content.